Applications of graphene in nanotechnology : 1D diffusion, current drag and nanoelectrodes

Vrbica, S.

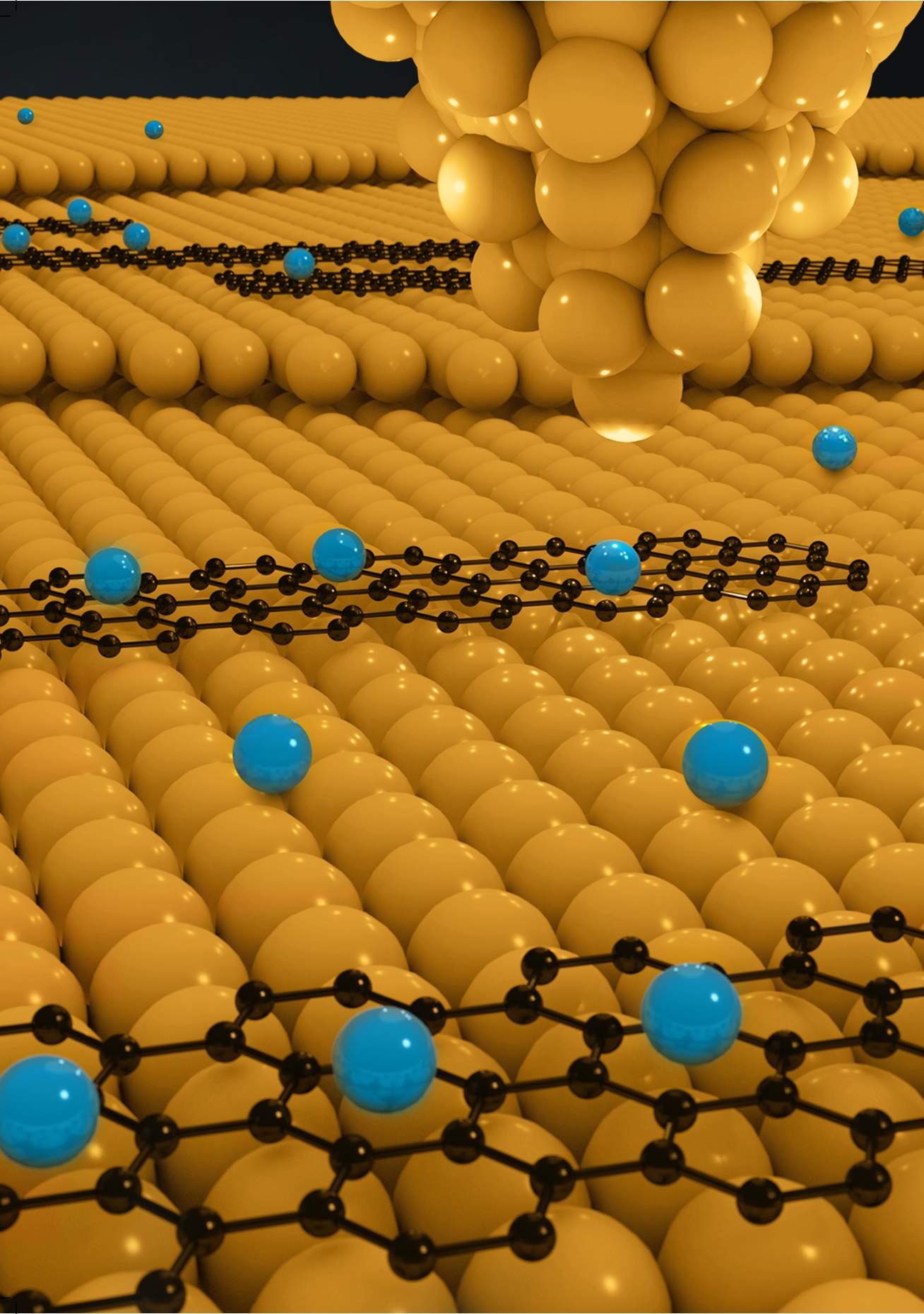

2

One-dimensional diffusion of Co adatoms on graphene nanoribbons

It is well known that a flow of electrons through a conductor exerts a force on atoms, which can lead to their displacement. The induced motion of atoms includes two mechanisms: stochastic thermal motion from heat and directional motion from the electron current. In order to allow for a quantitative comparison to theory, the experiment needs to be conducted at the scale of single atoms or single molecules. Here we utilize graphene nanoribbons (GNR) on Au(111) as a current-carrying substrate to demonstrate one-dimensional diffusion of single Co adatoms, by applying voltage pulses with a tip of a low-temperature scanning tunneling microscope (STM). The motion of single adatoms is traced by scanning the surface before and after the voltage pulses. We show statistics for Co displacements for different voltage amplitudes and different initial tip-adatom distances. Our observations reveal that migration of Co is mainly a thermally driven effect. Finally, we compare the data for Co on GNR to the statistics for induced motion of Co on Au(111) and discuss temperature-dependent diffusion measurements, which give information on relative diffusion barriers on GNR and Au(111).

The work is done in collaboration with - Irene Battisti[1], Ranko Tošković[2], Sander Otte[2], Tobias Preis[3], Nemanja Kocić[3], Jascha Repp[3] and Jan M. van Ruitenbeek[1]

[1]Huygens-Kamerlingh Onnes Laboratorium, Leiden University, The Netherlands.

[2]Otte Lab , Delft University of Technology, The Netherlands.

[3]Repp group, University of Regensburg, Germany.

2.1. INTRODUCTION

A voltage applied across a metal or a semiconductor leads to the displacement of the atoms from their positions in a crystal lattice. This phenomenon is known as electromigration and was first reported in 1861, when Gerardin observed motion of mass in molten alloys of lead-tin and mercury-sodium [1]. Theoretical and experimental work has established that the driving force for electromigration can be separated into contributions arising from the electron wind force ($\mathbf{F}_w$) and direct force ($\mathbf{F}_d$) [2–5]:

$$\mathbf{F}_{em} = \mathbf{F}_d + \mathbf{F}_w = (Z - nl\sigma)e\mathbf{E} \tag{2.1}$$

where Z is the charge of the adsorbate, n is the electron density, l is the electron mean free path, σ is the scattering cross section, e is the electron charge and $\mathbf{E}$ is the vector of external DC electric field. In this ballistic model a direct force is taken to be the applied electric field acting on the unscreened ion. The wind force is calculated from the rate of momentum transfer to the ion by the incident electrons. The electrons are treated in the free-electron gas model and the migrating ions are treated as impurity defects[1]. In this approximation, the direction of the wind force coincides with the direction of the electron current. If the net charge of the atom is positive, the direct force acts in the direction opposite of the electron current flow (Figure 2.1). The direction of atom diffusion will depend on the relative magnitudes of these two forces.

Electromigration is known to be the cause of failure of integrated circuits in microelectronics due to the formation of voids and hillocks in the wires [6–13], which poses a limitation on the maximum allowed power through the device (an example is shown in Figure 2.2(a) [13]). Numerous experiments have been performed on various current-carrying substrates in an attempt to learn more about the nature of the effect [14–17]. Initial experimental studies were limited to the collective motion of many atoms or the statistical description of large ensembles. Several decades of experimental work led to the utilization of electromigration for purification of bulk metals [18], controllable atomic-scale mass transport along the surface of a conduc-

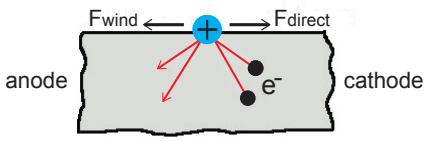

Figure 2.1: **Schematic illustration of two components of electromigration force.** Black balls represent electrons and a blue ball represents a positively charged atom.

[1] Note that this is a simplified model; more advanced descriptions can be found in the review by Sorbello[5]

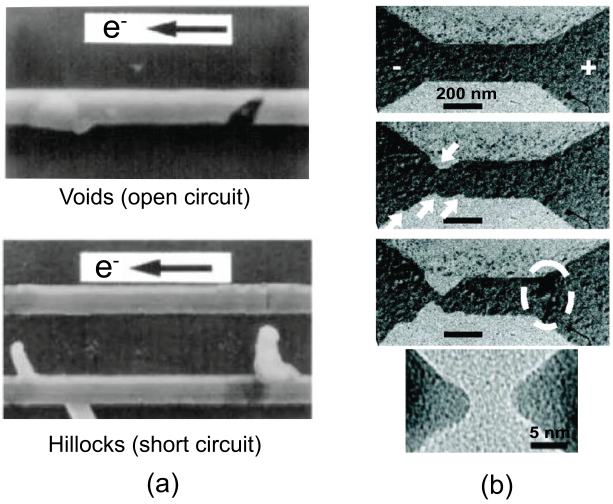

Figure 2.2: **Examples of destructive and constructive effects of electromigration.** (**a**) Scanning electron microscopy image of a circuit malfunction due to formation of voids (which lead to open circuit) and hillocks (lead to short circuit) in the wires [13]. (**b**) Electromigration-induced formation of gold nanoelectrodes [23]. After ramping a bias voltage across the 12 nm thick gold wire, voids form at the cathode side (arrows in the second image) while hillocks can be observed at the anode side (circle in the third image). Fourth image shows breaking of the device and formation of a 5 nm gap.

tor [19, 20] and the creation of nanoelectrodes for charge transport studies of individual molecules [21–26]. Figure 2.2(b) shows an example of electromigration-induced fabrication of gold nanoelectrodes on insulating Si_3N_4 membranes [23]. The electromigration process is induced by ramping up a voltage across a 12 nm thick gold wire of 600 - 800 Ω resistance, and starts when the current is of the order of a few milliamperes. Voids form at the cathode side of the wire (indicated by arrows in the second panel) while hillocks are formed at the anode side (circled area in the third panel). The wire narrows down as a function of time and eventually breaks along the grain boundary with a final gap size of 5 nm (fourth panel).

Recent experiments have begun to address the process of electromigration at the nanoscale. Métois *et al.* [27] observed motion of silicon islands of a single atom height on flat terraces along or against the current direction. Tao *et al.* [28] have shown displacement of monoatomic islands of 2 - 50 nm radius on a single-crystal Ag(111) in the direction of electron flow when current is passed through the substrate. The atomic-scale fluctuations at a step edge on a Ag single crystal are directly correlated to the electron wind force [29]. Electromigration is also used to induce motion of the material deposited on the surface of the conductor. As the atoms on the surface (so-called “adatoms”) have smaller binding energy, they are most likely to be electromigrated. Regan *et al.* [19] have demonstrated reversible mass transport of

indium nanoparticles of 50 - 100 nm size along multiwalled carbon nanotubes which are connected to the metal tip on one side and to the sample holder on the other side. By applying a voltage of a few volts between the tip and the sample holder, a current of ~ 50 μA is established and mass transport between indium nanoparticles along the nanotubes is induced. In one of the first experiments involving single-atom electromigration, Braun *et al.* [30] showed that single Au and Ag adatoms on a Ni(111) surface can be moved by electromigration forces from a scanning tunneling microscope tip. Depending on the amplitude and polarity of the applied bias voltage, atoms are either pulled towards the tip or pushed away. In all the aforementioned experiments it was the voltage gradient, rather than the thermal gradient that determined the direction of mass transport.

Current theories of electromigration that aim for a microscopic description lack proper experiments for testing, and do not always successfully predict the extent and the direction of atom diffusion. Girard *et al.* [31] show in their theoretical study that certain types of adatoms (oxygen (O), fluorine (F) and nitrogen (N)) move under the influence of current-induced forces along a carbon nanotube in the direction of electron flow, while the other adatoms (boron (B) and carbon (C)) move in the opposite direction. The authors argue that there is a loose correlation between the atomic charge of the adsorbates and the direction and strength of the forces. O, F and N are negatively charged and the forces acting on them are in the direction of the electron flow, while B and C are positively charged and are pulled against the electron flow. This directionality indicates the dominance of the direct force over the wind force for these particular adsorbates. Solenov *et al.* [32], on the other hand, show that according to a tight binding model of electromigration of an adsorbate on graphene, the electron wind contribution dominates the electromigration force (except for the smallest Z or low conductivity). A deeper understanding of current-induced forces is necessary for a proper description of electromigration.

2.1.1. NON-CONSERVATIVE WIND FORCE AND BERRY FORCE

One of the holy grails of nanotechnology is the realization and utilization of autonomous nanomachines. A concept of a *molecular waterwheel* - a nanomotor driven by means of a direct current flow (in analogy to a waterwheel driven by a water flow) - is very appealing since it would not require externally supplied cyclic driving. In order to achieve this state, a non-conservative force is required to act between the non-equilibrium electron bath and ions comprising the nanoscale system so that net work is done per revolution. In a recent theoretical paper, Dundas *et al.* [33] analytically showed that the current-induced forces in atomic wires are non-conservative and can, in principle, be used to drive molecular machines. This gives a whole new outlook on the nature of electromigration. The concept of non-conservative wind force was further elaborated in works of several research groups [34–38]. Subsequently, Lü *et al.* [39] showed that interactions between the electrons and the lattice

give rise to another component of electromigration force, the so-called *Berry force*. This force originates from the change of phase (*Berry* phase) of the electronic wave functions due to the atomic motion, and acts just like a Lorentz force: it is perpendicular to the velocity of the ions and keeps them in periodic orbits. Both contributions to the force appear only when the electron gas is driven out of equilibrium (e.g. in the presence of the current flow) and can lead to instabilities (so-called *runaway* modes) that can effectively displace atoms. Truly microscopic experiments probing these forces at the scale of single atoms or molecules have not yet been conducted. The first promising data has been reported recently by Schirm *et al.* [40] on aluminum chains and by Sabater *et al.* [41] on Au and Pt atomic chains, both performed with mechanically controlled break junction techniques.

In the interest of giving a proper description of the electromigration force and closing the gap between theory and experiment, an experiment needs to be designed at the scale of single atoms or single molecules in order to trace their individual motion. In this chapter we start with a brief discussion on graphene as a current-carrying substrate, followed by a description of experimental setups and sample preparation techniques. We report on one-dimensional migration of single Co adatoms along graphene nanoribbons, induced by voltage pulses applied on the nanoribbons with a tip of a scanning tunneling microscope (STM). We are able to trace the motion of Co by scanning the surface of the sample before and after voltage pulses. Later in section 2.8.2 we discuss the migration of Co on the underlying Au(111) surface and compare it to the statistics obtained for the motion of Co on nanoribbons. Finally, we present temperature-dependent diffusion measurements and draw conclusions on the effects of the current on the migration of Co adatoms.

2.2. GRAPHENE

Graphene – a single layer of graphite – is a two-dimensional carbon allotrope with carbon atoms arranged in a hexagonal lattice. It was first isolated in 2004 by Geim and Novoselov [42] for which they were rewarded a Nobel prize a few years later. Graphene efficiently conducts heat and electricity [43] and its strong in-plane σ bonds make it one of the strongest materials ever tested [44]. Graphene is also a good candidate for a current-carrying substrate for investigating current-induced forces. It can withstand very high currents while in vacuum without suffering damage and its 2D nature enables a confinement of the current within the atomically thin layer, in contrast to 3D materials where a large portion of the current flows into the bulk. The flat surface of graphene enables the observation of single adatoms deposited on top of it and tracking of their migration under the influence of the current.

2.2.1. GRAPHENE NANORIBBONS (GNRS)

Grahene nanoribbons (GNRs) are strips of graphene that can be fabricated with precise widths from chemical precursors. Their electronic and magnetic properties can be fine-tuned by choosing the appropriate width and edge geometry, enabling the fabrication of semiconducting or metallic GNRs. Figure 2.3 shows GNRs with zigzag (a) and armchair (b) edges. Zigzag GNRs are predicted to be half-metallic [45] and reveal spin-polarized edge states [46]. Armchair GNRs (AGNR) can be grouped into three families: $N = 3p$, $N = 3p+1$ and $N = 3p+2$, where p is an integer and N is the number of carbon atoms along the GNR width. $N = 3p$ and $N = 3p+1$ families have wide bandgaps that decrease with the increase of the ribbon width [47–50]. Models predict the family $N = 3p+2$ to be metallic [47, 51]. Using GNRs is advantageous compared to using graphene for reasons that will become apparent in later sections.

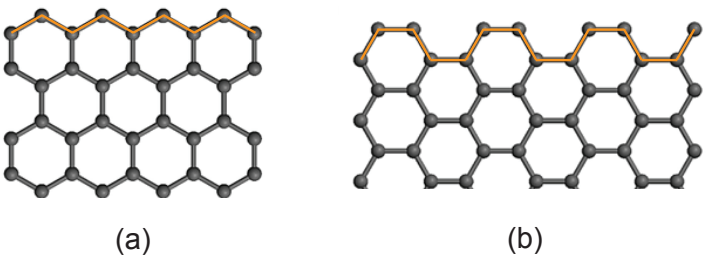

Figure 2.3: **Two different edges of a graphene nanoribbon.** (**a**) Zigzag and (**b**) armchair edge.

2.3. SCANNING TUNNELING MICROSCOPY

In classical mechanics current cannot flow in an open circuit when the potential barrier of the gap between two conductors is higher than the energy of the electrons. In quantum mechanics, however, electrons are presented with the wave function which decays exponentially within the insulating gap. If the gap is narrow enough, the wave function will reach the other electrode and there will be a nonzero probability for electrons to tunnel through the barrier.

In 1981 Binnig and Rohrer from the IBM Zurich Research Laboratory invented Scanning Tunneling Microscope (STM) based on the concept of quantum tunneling [52]. It was one of the first instruments ever to directly image the topography of a sample with atomic resolution. A probe (tip), usually made of a Au or Pt-Ir alloy wire, is brought into the vicinity of the sample [2] by means of a piezo actuator (Figure 2.4(a)). By applying a positive bias voltage to the sample with respect to the tip (V_b),

[2] Typically at around 1-2 nm distance

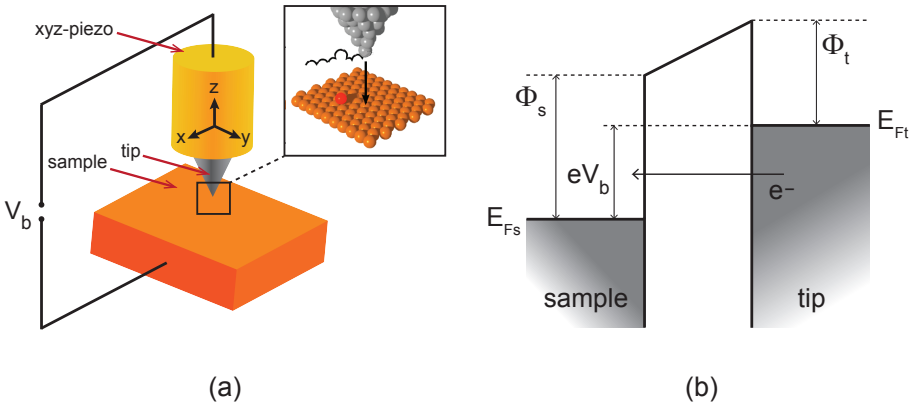

Figure 2.4: **Basic principle of STM.** (**a**) Schematics of a tip scanning over the surface of the sample with bias voltage V_b applied between them. A high voltage applied to the piezo actuator (yellow cylinder) serves as a feedback to keep the tunneling current constant. (**b**) Energy levels of a one-dimensional tunneling barrier. When a bias voltage is applied, tip states between the energy levels E_{Ft} – eV and E_{Ft} (Fermi energy of the tip) can tunnel to the sample, generating a tunneling current proportional to V_b.

electrons with the energy between E_{Ft} – eV_b and E_{Ft} (Fermi energy of the tip) can tunnel from occupied states in the tip to unoccupied states in the sample, generating a net tunneling current[3] (Figure 2.4(b)). The tunneling current exponentially decays with the distance z between the sample and the tip as

$$I \propto V_b\, e^{-kz} \tag{2.2}$$

where V_b is bias voltage and k is a decay constant of the tip state near the Fermi level in the barrier region. In the approximation $eV_b << \phi$, k can be expressed as

$$k = \frac{\sqrt{2m_e\phi}}{\hbar} \tag{2.3}$$

where m_e is the mass of electron, ϕ is the work function of the tip and sample, and $\hbar$ is the reduced Planck constant. In general, the work function depends not only on the material but also on the crystallographic orientation of the surface[4].

In constant-current mode, the tunneling current is amplified and converted to voltage by the current amplifier and then compared with the reference value (set-point). The difference is then amplified to drive the Z-piezo and control the tip-sample distance in order to maintain the setpoint current. This is known as the feedback loop. As the tip scans over the surface of the sample line by line in a raster-like fashion, a Z displacement given by the high voltage applied to the piezo actuator is

[3] For negative bias voltage, tunneling current will flow in the opposite direction

[4] For typical values of the work function of a metal (around 5 eV), change of the tip-sample distance by 0.1 nm results in an order of magnitude change in tunneling current

recorded. The recorded array of equilibrium Z positions is then displayed as a height image of the sample surface. Bright spots represent high z values (protrusions), and dark spots represent low z values (depressions). The contrast in STM images does not depend only on the topography of the sample surface, but also on the electronic structure of the sample[5]. Measurements with STM in ultra-high vacuum environment at low temperatures can yield atomic resolution imaging and spectroscopy.

All experiments in this chapter were carried out with an STM technique using three different types of STM described in section 2.5.

2.4. ATOMIC FORCE MICROSCOPY AND KELVIN PROBE FORCE MICROSCOPY

Atomic Force Microscopy (AFM) is another surface imaging technique invented by G. Binnig *et al.* [53]. AFM does not require a conductive probe and sample, as it measures the force between them. The AFM used in experiments in this chapter is based on piezoelectric properties of the mechanical actuator (quartz tuning fork) which serves as the force sensor [54]. In non-contact AFM, the mechanical actuator is excited to oscillate at its resonance frequency f_0. As the tip on the tuning fork approaches the sample and feels an attractive or repulsive force, a feedback loop ensures that the tuning fork oscillates with a constant amplitude. The deflection signal is routed through a bandpass filter, phase shifted and fed back to the actuator. A phase-locked loop determines the oscillation frequency $f = f_0 + \Delta f$, and the frequency shift Δf is used as the signal.

We used AFM to determine a difference in work functions between the sample and the tip (Figure 2.5). When two bodies are in electrical contact, electrons flow from the metal with the higher Fermi energy (lower work function Φ), to the one with the lower Fermi energy (higher Φ), until Fermi levels are aligned (Figure 2.5(b)). The accumulated negative charge on one electrode will attract positive charges in the other, creating an electric field within the gap, hence an extra attractive force. By applying appropriate bias voltage between sample and tip, the electric field is canceled and the situation from panel (a) is restored (Figure 2.5(c)). The voltage required to minimize electrostatic interaction is given by

$$V_b^* = \frac{1}{e}(\Phi_s - \Phi_t) \tag{2.4}$$

The concept of detecting differences in work functions via the electric field between two electrodes was introduced by Lord Kelvin [55]. Kelvin probe force microscopy (KPFM) uses the force between the sample and the oscillating probe (tip) as a signal. This is done by keeping the tip at a fixed position while sweeping the

[5] For this reason one usually refers to feature sizes in STM images as *apparent* height and width

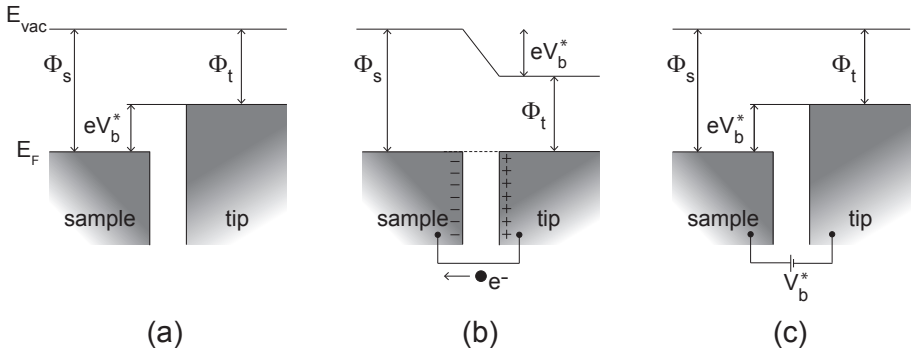

Figure 2.5: **Energy levels of two metallic surfaces facing each other.** (**a**) No electrical connection between sample and tip. Vacuum levels are aligned while the Fermi energies are not, due to the difference in work functions of the sample and the tip (Φ_s and Φ_t, respectively). (**b**) Sample and tip are electrically connected. Electrons flow to the electrode with higher work function until the Fermi energies align. This charge transfer causes an electric field between the sample and the tip. (**c**) By applying an appropriate bias voltage, V_b^*, the contact potential difference is compensated and the electrostatic interaction is minimized.

bias voltage and recording the frequency shift, Δf, caused by the electrostatic interaction between the sample and the tip. The $\Delta f(V)$ spectrum is known as the Kelvin parabola. For a certain value of the bias voltage V_b^*, the electrostatic interaction between the sample and the tip will be minimized and the frequency shift will reach its extremum. The bias voltage of minimal interaction provides a qualitative measure of the difference in work functions between the sample and the tip.

2.5. EXPERIMENTAL SETUPS

2.5.1. JEOL ROOM-TEMPERATURE UHV STM

Initial experiments on CVD graphene were performed in a JEOL ultra-high vacuum Scanning Tunneling Microscope (UHV STM) operating at room temperature (Figure 2.6). The setup consists of three separate chambers: load-lock, preparation chamber and STM chamber. The sample and tip holders are introduced from the load-lock to the preparation chamber with a short transfer arm. The preparation chamber is equipped with a heater for sample preparation. The scan head is located in the STM chamber at a pressure of $1{\cdot}10^{-9}$ mbar. Sample holder is mounted on a piezo tube with a 2 μm range of motion along X and Y directions. The sample holder has two electrical contacts for the placement of current through graphene. The STM tip is a 200 μm gold wire.

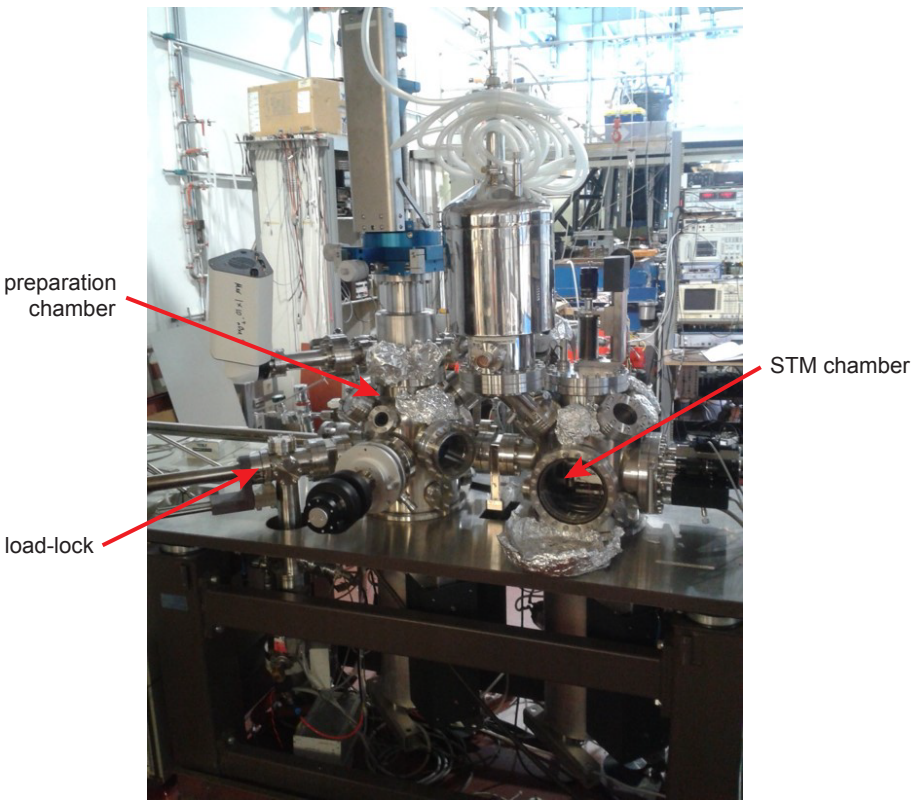

Figure 2.6: **JEOL room temperature UHV STM/AFM.** The setup consists of three independent chambers: load-lock, preparation chamber (with a heater) and STM chamber.

2.5.2. SPECS LOW-TEMPERATURE UHV STM

A part of experiments on CVD graphene were performed in a low-temperature SPECS Joule-Thomson UHV STM (Figure 2.7) in Delft, in the group of Sander Otte. The operating temperature is 10 K and the pressure is $7{\cdot}10^{-11}$ mbar. The sample holder in this STM also has two contacts for placement of current through graphene. As a tip we used either a chemically etched tungsten wire or PtIr wire.

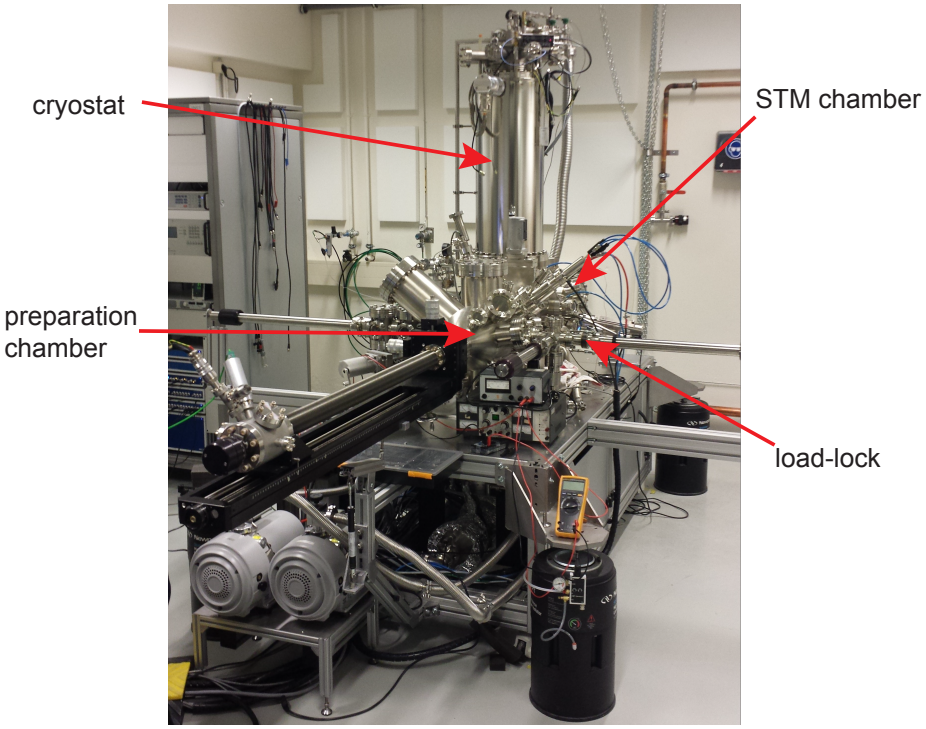

Figure 2.7: **SPECS Joule-Thomson low temperature UHV STM.** The setup consists of three independent chambers: load-lock, preparation chamber and STM chamber. The sample is inserted into the load-lock and transferred to the preparation chamber. An evaporator is situated in the preparation chamber and evaporation is done *in situ* directly onto the cooled sample.

2.5.3. CREATEC LOW-TEMPERATURE UHV STM

The majority of the experiments in this chapter were carried out using a low-temperature UHV combined STM/AFM system, which is a modified version of a commercially available instrument from Createc Fischer & Co. GmbH® (Figure 2.8(a)) at the University of Regensburg in the group of Jascha Repp.

The setup consists of three separate chambers: load-lock, preparation chamber and STM chamber. The preparation chamber is equipped with a sputter gun for

sample preparation. A quartz sensor for molecular deposition and evaporators for atomic and molecular evaporation are introduced from the load-lock with a transfer arm. The scan head is located in the STM chamber under the liquid helium bath cryostat at 7-10 K at a pressure of P = $5 \cdot 10^{-11}$ mbar.

The STM scan-head is based on the Besocke beetle design [56, 57] shown in Figure

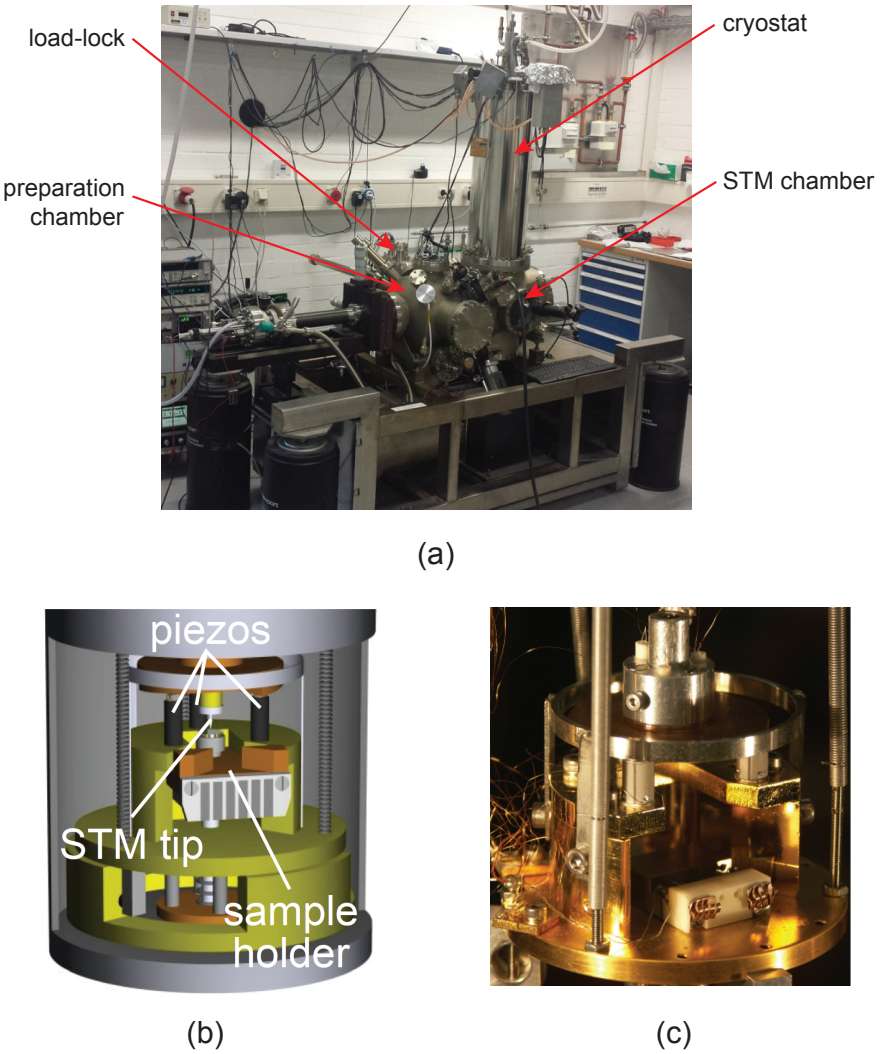

Figure 2.8: **Createc low temperature UHV STM/AFM.** (**a**) The setup consists of three independent chambers: load-lock, preparation chamber and STM chamber. The sample and evaporators are inserted into the load-lock and transferred to the preparation chamber. (**b**) Schematics of the STM/AFM scan head based on the Besocke beetle design. (**c**) Photograph of (b) without the sample holder inside.

2.8(b), (c). The STM tip is attached to a disk which rests on three sapphire balls glued to three piezo tubes. By applying a saw-tooth voltage pulses to the electrodes of the piezo tubes, the disk is rotated using the principle of a slip-stick motion. Since the disk has three slightly inclined planes on the bottom side, motion of the piezos results in a vertical motion of the tip. The scan-head is suspended by three springs and equipped with an eddy current damping system.

2.6. FIRST EXPERIMENT: CVD GROWN GRAPHENE ON SI/SiO_2 IN ROOM-TEMPERATURE JEOL STM

Initial experiments were performed in the JEOL room-temperature UHV STM using CVD grown graphene on a Si/SiO_2 substrate purchased from Graphenea®. The SiO_2 thickness of 285 nm serves to separate graphene electrically from Si in order to ensure confinement of the current within the graphene sheet and the thickness is such that single-layer graphene deposited on top of it can be detected optically.

Graphene was covered with a layer of poly(methyl methacrylate) polymer (PMMA) and patterned with electron-beam lithography in order to obtain a 300×300 μm^2 graphene patch. In a second lithography step, electrodes were patterned and graphene was further contacted with a 5 nm thick adhesion layer of chromium and a 100 nm thick layer of gold deposited by thermal evaporation (Figure 2.9(a)). The sample was subsequently placed inside a JEOL room-temperature ultra-high vacuum scanning tunneling microscope (UHV STM) in order to image the surface of the graphene. However imaging of the sample was obstructed due to the presence of unavoidable PMMA residues on the surface of the graphene, even after thorough cleaning with acetone. The STM tip was continuously crashing while scanning over the parts covered with insulating polymer. *In situ* thermal annealing of the sample at 280°C for 6 hours reduced the noise level in the current signal, however the sample remained contaminated by the organic residue and the graphene lattice was not observed.

As a solution for cleaning the sample, we employed the current-induced cleaning procedure of graphene by Moser *et al.* [58], where they introduce a current density of 10^8 A/cm^2 into exfoliated graphene in ambient conditions, in order to remove contaminants deposited during lithography. The effects of a large electrical current passing through a graphene sheet include Joule heating, evaporation of nanoparticles due to high temperatures and possibly electromigration of material. Injection of the current of 3 mA (which translates to a current density of around $3{\cdot}10^6$ A/cm^2) into the graphene via two gold contacts for the duration of 1 hour resulted in the removal of a large fraction of PMMA residue from the surface, and atomic resolution was achieved (Figure 2.9(b)). It should be noted that the sample was not perfectly clean even after all the above-mentioned cleaning procedures, which was noticeable in the STM images.

After confirming that surface of graphene can be cleaned using the current-cleaning

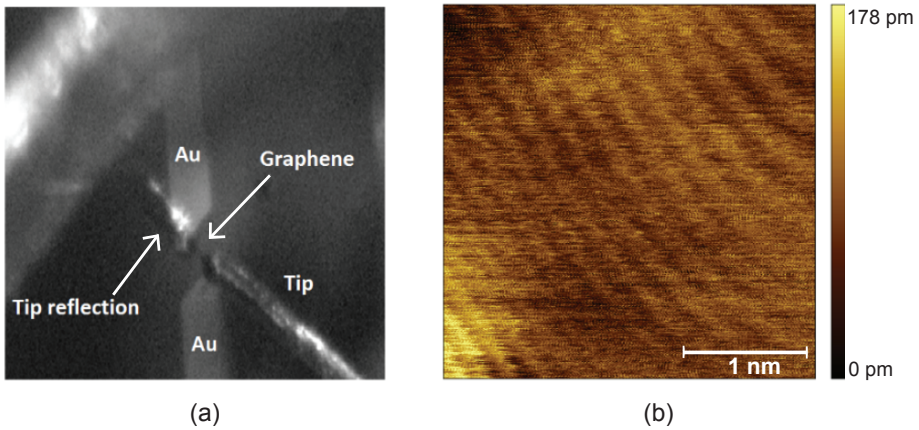

Figure 2.9: **Graphene patterned with e-beam lithography** (300×300 μm^2). (**a**) Optical microscope image of the sample and the tip positioned inside the JEOL UHV STM at room temperature. (**b**) Atomic resolution of graphene after current-cleaning procedure.

technique, we proceeded with experiments in the low-temperature STM. Single adatoms are mobile at the room temperature and the sample has to be cooled down in order to avoid any thermal motion before inducing electromigration.

2.7. SECOND EXPERIMENT: CVD GROWN GRAPHENE ON SI/SiO_2 IN LOW-TEMPERATURE SPECS STM

After confirming that the current-cleaning procedure was successful in removing the majority of polymer residue off the surface of the graphene, we have made an attempt to induce electromigration inside a SPECS® low-temperature UHV STM. The position of the camera on the STM chamber which gave visual access to the position of tip with respect to sample was a limiting factor in the size of the graphene, as it would be hard to approach the tip to the sample on a small graphene patch without the tip crashing onto the insulating SiO_2. We used 5×5 mm^2 CVD graphene on copper purchased from Graphenea®, which we transferred to a Si/SiO_2 substrate (with 285 nm oxide thickness). The graphene patch was contacted with chromium and gold as described earlier, giving a resistance of 15 kΩ. After passing a current of I = 5.2 mA in the graphene for 20 min as a cleaning procedure, the sample was cooled down to 10 K and subsequently scanned (Figure 2.10(a)). First, in this high-resolution image (note the scale) we recognize the hexagonal graphene lattice structure throughout the image, demonstrating that the surface is mostly clean. Second, the surface does not appear flat, there is a modulation of the height with a cloudy-like

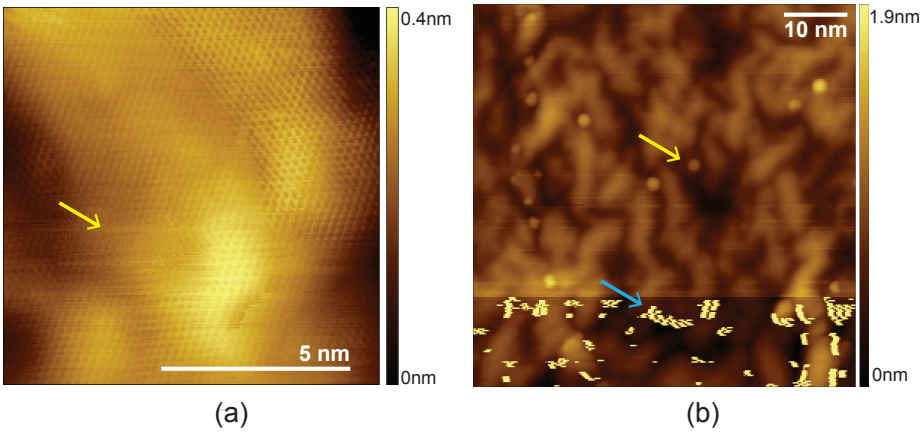

Figure 2.10: **STM images of graphene before and after evaporation of Co adatoms.** (**a**) Graphene on SiO_2 after current cleaning at high resolution (note the scale bar of 5 nm). Graphene appears to be relatively clean in the upper half of the image until the onset of horizontal stripes (indicated by yellow arrow). Scanning parameters: V = 1 V, I = 100 pA. (**b**) Graphene surface imaged over a wider area (scale bar 10 nm) after *in situ* evaporation of cobalt. Co adatoms appear as bright round shapes (the yellow arrow points at one of the Co adatoms or clusters). Small bright patches that appear in the bottom of the image (indicated by the blue arrow) are most likely dirt that comes from polymer residues and that the tip picked up. The images were obtained at 10 K. Scanning parameters: V = 2 V, I = 30 pA.

structure. This cloudy structure is usually attributed to the SiO_2 surface roughness [59], possibly in combination with random structure of charge traps in the Si/SiO_2 substrate. Graphene appears to be relatively clean in the upper half of the image until the point indicated by the yellow arrow, after which horizontal stripes can be observed. Their appearance suggests that the sample is not quite clean, and that the tip picks up dirt and changes as it scans along the horizontal line.

Cobalt atoms were evaporated *in situ* on cold graphene via e-beam heating. Figure 2.10(b) shows graphene after Co evaporation. Co adatoms or clusters appear as bright round shapes (the yellow arrow indicates one of the adatoms or clusters). Small bright irregular patches in the bottom of the image (indicated by the blue arrow) are attributed to dirt that the tip picked up during the scan, and they are present in the majority of the scans. In this particular experiment we did not have means to clean the tip, since the usual tip indentation into a clean patch of a Au metal surface was not an option. A current of I_{max}= 9 mA (which corresponds to around $5 \cdot 10^5$ A/cm^2 current density) was applied through graphene for t = 17 min. This was the maximum current that the STM wires were designed to carry. We observed no motion of Co adatoms, which indicates that the current density was not sufficient to induce electromigration. A possible reason for the lack of motion of adatoms could be that Co adheres more strongly to graphene/SiO_2 than the polymer does.

Considering the practical limitations of using CVD graphene, such as limitations

in achievable current density, limitations imposed by the corrugation of the SiO_2 substrate and limitations in cleaning of adsorbents and other defects, we concluded that graphene is not the most suitable material for our experiment. We decided to proceed with an alternative substrate: graphene nanoribbons.

2.8. THIRD EXPERIMENT: GRAPHENE NANORIBBONS IN LOW-TEMPERATURE CREATEC STM

In contrast to CVD graphene, the surface of graphene nanoribbons (GNRs) is free of contaminants since there is no polymer involved in the preparation procedure and the growth of GNRs takes place under UHV conditions. The growth substrate has to be a metal (usually Au, Ag or Cu), since it serves as a template and catalyst for the surface-assisted synthesis step.

A single crystal of Au(111) was cleaned by Ne^+ ion sputtering at the pressure of 10^{-5} mbar, followed by thermal annealing at 550°C. The procedure for growth of GNRs on Au(111) is reproduced from the work of Cai *et al.* [61]. We used 10,10′ − dibromo−9,9′−bianthryl (DBBA) molecules (Figure 2.11(a)) as precursors to produce armchair-edge graphene nanoribbons. DBBA was evaporated for 3-7 sec at a distance of around 1.5 cm from the sample. Thermal sublimation of DBBA onto the Au(111) surface kept at 100°C resulted in dehalogenation (removal of bromine atoms from DBBA molecules). In the first thermal activation step, the temperature was increased to 220°C and kept constant for 2 min, during which monomers diffused across the surface to covalently bond with other monomers by fusion of the bonds, exposed by the release of Br. This resulted in a formation of non-planar polymer chains (Figure 2.11(b)). In the second thermal activation step, the temperature was further increased to 410°C and kept constant for 3 min, inducing an intramolecular cyclodehydrogenation of the polymer chains and formation of armchair GNRs (Figure 2.11(c)).

As a tip we used a 20 μm thick PtIr wire. The tip was prepared by controlled crashes onto the clean gold surface with the feedback on and 10^6 amplifier gain, which resulted in atomically sharp gold-coated STM tip. Figure 2.12 shows a Kelvin parabola $\Delta f(V)$ (discussed in subsection 2.4). The value of the bias voltage that corresponds to the minimum of Δf is around 500 mV. The bias voltage is applied on the sample while the tip is virtually grounded, therefore the work function of the sample is 500 meV higher than the work function of the tip.

In addition to KPFM, we used AFM to detect when the tip would become blunt and perform a new cycle of tip preparation. Determining the shape of the tip was done by comparing the oscillation frequency of the tip when it is positioned far away from the sample (out of tunneling) to the frequency of the tip in the vicinity of the sample. For a wide (blunt) tip the frequency shift is large due to a large interaction of the tip with the sample (~ 25 Hz). For a good, sharp AFM tip the frequency shift is

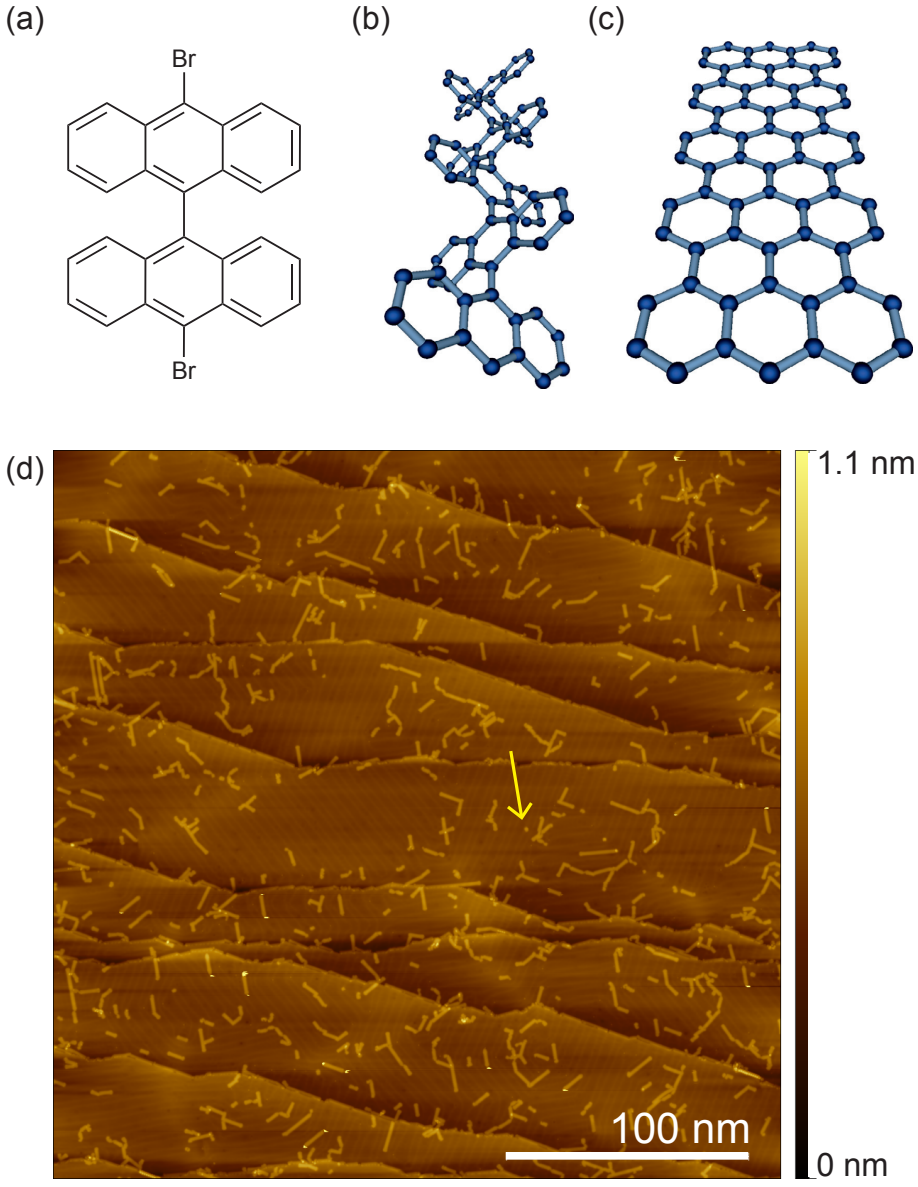

Figure 2.11: **Bottom-up fabrication of 7-armchair GNRs.** (**a**) Chemical structure of a 10,10′ -dibromo-9,9′ -bianthryl (DBBA) precursor molecule [60]. (**b**) C-C covalent bonding and formation of a linear polymer during the first annealing step. (**c**) Formation of a 7-AGNR as a result of cyclodehydrogenation during the second annealing step. (**d**) STM image of the sample after GNR formation on Au(111) (V_b = 100 mV, I = 1.1 pA). The bright worm-like structures scattered over the surface are the GNRs. Small square-like bright features are single precursor molecules (indicated by the yellow arrow).

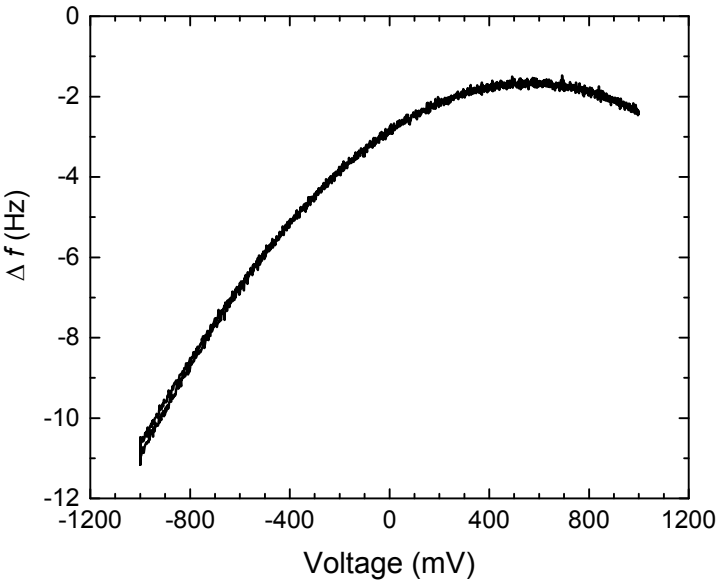

Figure 2.12: **Kelvin probe force microscopy (KPFM) measurement.** The maximum of the curve (i.e. the minimum of $\Delta f(V)$) corresponds to approximately 500 mV bias voltage.

around 5 Hz.

An STM image of the sample after the formation of GNRs is shown in Figure 2.11(d). Small square-like bright features are single precursor molecules (indicated by the yellow arrow), while the elongated rectangular or worm-like structures are the GNRs. The lengths of the GNRs range from 2 to 40 nm.

As the next step we performed *in situ* evaporation of cobalt (Co) on the sample via electron beam evaporation. Co was evaporated at a distance of around 15 cm for 5 sec, while the high voltage was at 2 kV and the emission current read out was 2 mA. An STM image of the sample after Co deposition is shown in Figure 2.13(a). Co adatoms on Au(111) appear as small bright round shapes with the apparent height of 0.2 nm and a diameter of ~ 0.5 nm. As a first important observation we notice that a significant fraction of Co atoms reside on top of GNRs. Co adatoms on a GNR appear much bigger, with the apparent diameter of 1.5 - 2 nm [62] (see the linear height profile in the inset in Figure 2.13(b)).

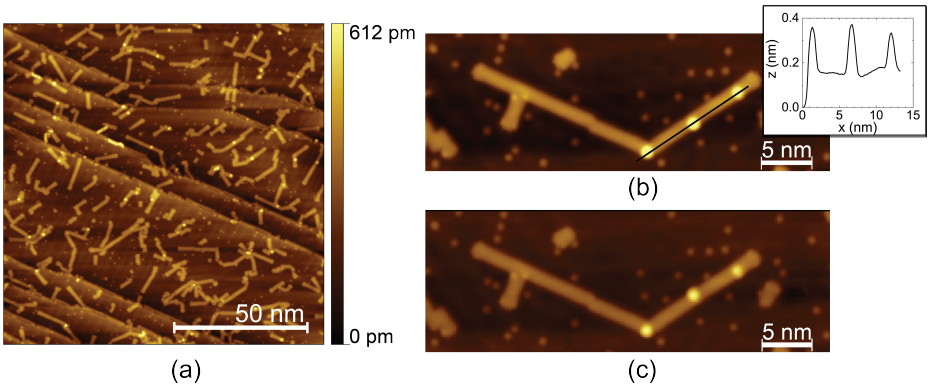

Figure 2.13: **Sample after Co evaporation.** (**a**) Large-area STM image of the sample after cobalt evaporation (V_b = 0.1 V, I = 2 pA). (**b**) STM image of a GNR with three Co adatoms on top (V_b = 0.3 V, I = 1.6 pA). Co adatoms on a GNR appear bigger than Co adatoms on a gold surface. The inset shows a line profile along one arm of a GNR indicated by the black line in the main panel. (**c**) STM image of the same GNR after tip manipulation. The middle Co adatom moved laterally from the right to the left on the GNR.

Co adatoms can be found in different lateral positions on the GNR (Figure 2.13(b), (c)). DFT calculations for Co adatoms on a graphene sheet indicate that the stable adsorption site for Co is the center of the GNR hexagon [63], which suggests five possible lateral positions (blue dots in Figure 2.14). We cannot distinguish all five positions within the STM resolution (~ 0.2 nm).

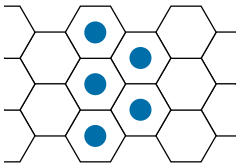

Figure 2.14: **Possible lateral adsorption sites for Co adatom on GNR (blue dots) [63].**

2.8.1. CURRENT-INDUCED MANIPULATION OF CO ADATOMS

The GNRs of interest are 5-20 nm long, do not cross other GNRs and have 1−7 Co adatoms on top. These criteria were chosen in order to ensure the best possible conditions for tracking of Co adatoms after injection of the current. Migration of Co adatoms on a GNR was induced by applying voltage pulses while the tip was brought into point contact with the GNR. We used voltage pulses in the range of $-1000\ \text{mV} \leq V_b \leq -600\ \text{mV}$ and $600\ \text{mV} \leq V_b \leq 1200\ \text{mV}$ (voltage is applied on the sample while

the STM tip is grounded).

Increase of the current with decreasing tip−sample distance (z) in most cases had a smooth exponential trend up to 10 μA (the value at which the current amplifier saturates) without noticeable kinks in the slope that would indicate point contact between the tip and the GNR. In order to obtain the point-contact value, we first established a tip−Au(111) point contact on the Au surface near a GNR (which corresponds to R = 12.9 kΩ), then we lifted the tip by the height of the GNR (~ 0.2 nm) and positioned it above the GNR. The current read-out for this tip position showed values around 0.3−0.6 μA for 100 mV bias voltage (which corresponds to $R_{pc} \approx 250$ kΩ). This value was noted as the tip−GNR point contact and was used in all manipulation experiments. The point contact was also confirmed by observing a small kink in the current slope around 0.3−0.6 μA in some of the I(t) curves.

During the manipulation, the initial setpoint is set to I = 1−2 pA at V_b = 0.1 V. After switching off the feedback, the amplifier gain is reduced to 10^6 to enable recording of higher currents. The STM tip is brought closer to the GNR until the point contact value is reached. A voltage pulse is subsequently applied with a duration of 0.2−1 sec. The tip is then retracted, the amplifier gain is set back to 10^{11} and the feedback is switched on. Figure 2.15(a) shows an example of this procedure for a positive voltage

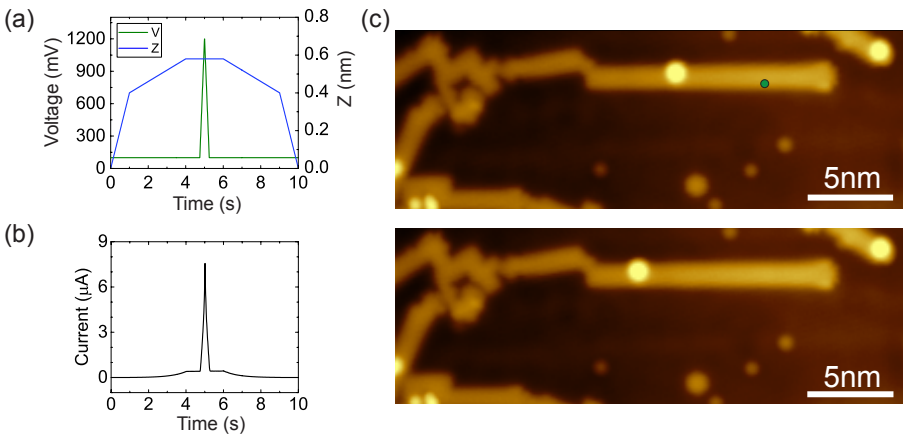

Figure 2.15: **Example of the motion of a single cobalt adatom along a GNR induced by a positive voltage pulse via the STM tip.** (**a**) The blue line represents the relative tip-sample distance (Z) with respect to the feedback setpoint position. Z increases as the tip goes towards the surface, until the point-contact position with a GNR is reached. Around 1 sec after the point-contact is established, a short voltage pulse of V_b = 1200 mV is applied (green line) and the tip is subsequently retracted by a procedure that is the reverse of the approach. (**b**) Current corresponding to the tip motion and voltage pulse from (a). At the initial bias of 100 mV, the value of the point-contact current between the tip and the GNR is around 0.3 − 0.6 μA. (**c**) STM images of a GNR before and after the voltage pulse of V_b = 1200 mV. The green dot on the GNR marks the position of the tip at the moment of the pulse after which the Co adatom has moved away from the tip, as observed in the lower image taken after the event.

pulse of V_b = 1200 mV (green line) and the corresponding Z-position of the tip with respect to the feedback setpoint position (blue line). Figure 2.15(b) shows the corresponding current. After the voltage pulse, the same sample area is scanned in order to trace any motion of Co adatoms.

STM images of the sample before and after a positive voltage pulse of V_b = 1200 mV on the GNR can be seen in Figure 2.15(c). The green dot marks the position of the tip at the moment of the pulse. After the voltage pulse, we observe that the Co adatom has moved along the GNR away from the tip.

An example of a negative voltage pulse of V_b = −900 mV and the corresponding current can be seen in Figure 2.16(a), (b), respectively. Figure 2.16(c) shows STM images of Co on a GNR before and after this negative voltage pulse of −900 mV (with the tip at the position marked by the red dot). In this particular case, the Co adatom is observed to have moved towards the tip after the pulse. Interestingly, we find that the atoms are displaced along the GNR and do not leave the GNR towards the Au(111) surface. We will discuss this confinement of Co adatoms to GNRs more extensively in the following sections.

Two GNRs can chemically bond to form a GNR with a bend. If the produced 7-AGNRs come into close proximity to each other, they can undergo cross-dehydrogenative coupling to form more complex structures [64, 65]. The work of Dienel *et al.* [66] offers a comprehensive characterization of the atomic connectivity in the 7-AGNR junctions on Au(111). Figure 2.17(a) shows an STM image (courtesy [66])

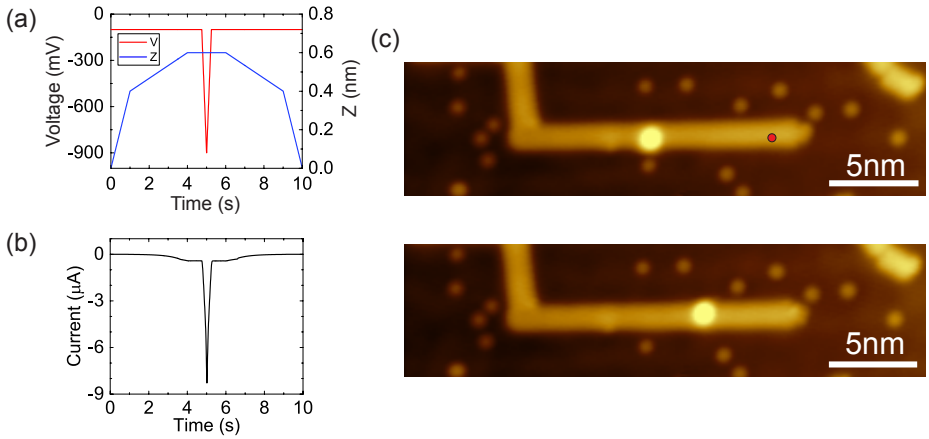

Figure 2.16: **Example of an induced motion of a single cobalt adatom on a GNR by a negative voltage pulse via the STM tip.** (**a**) The red line represents a negative voltage pulse of V_b = −900 mV with a duration of 0.5 sec. The blue line represents the relative tip-sample distance (Z) with respect to the feedback setpoint. (**b**) The current as a function of time. (**c**) Representative STM images of a GNR before and after a voltage pulse of V_b = − 900 mV. The red dot on the GNR marks the position of the tip at the moment of the pulse. The Co adatom is observed to have moved towards the tip after the pulse.

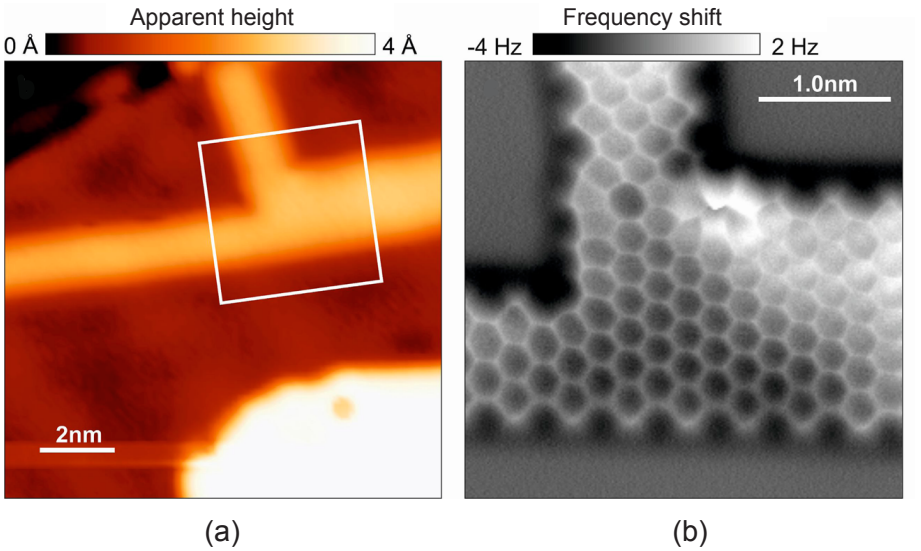

Figure 2.17: **Cross-dehydrogenative coupling of AGNRs.** (**a**) STM image (V_b = 0.2 V, I = 2 pA) of a junction between AGNRs of different widths on Au(111) (image taken with permission from [66]).(**b**) Constant-height non-contact AFM frequency shift image of the junction between two 7-AGNRs and one 14-AGNR shown in (b).

of a junction between two regular 7-AGNRs and a broader ribbon extending to the right. Figure 2.17(b) shows a non-contact AFM image in which one can distinguish the hexagonal rings within the two 7-AGNRs on the left and top edges of the image, and within the broad structure on the right. The broad structure is in fact a fully conjugated 14-AGNR formed by cross-dehydrogenative coupling of two 7-AGNRs along their long axis.

We find that Co adatoms can be manipulated even when the voltage pulse is applied around the bend of a GNR with such a kink. Figure 2.18 shows an example of a Co adatom manipulation on such a GNR. After a positive voltage pulse of V_b = 900 mV (at the position marked by the green dot in panel (a)) on the right part of the GNR, the Co adatom is pushed away from the tip along the path of the GNR (panel (b)). Furthermore, after applying a second, negative voltage pulse of $V_b = -1000$ mV (at the position marked by the red dot in panel (c)) the Co adatom moves along the GNR towards the tip (panel (d)). We have, however, not observed any motion of Co adatoms around the bend/corner of a GNR: once in the corner, Co adatom would not move along the GNR any longer after subsequent voltage pulses, suggesting that this position offers a local potential minimum for the Co adatom.

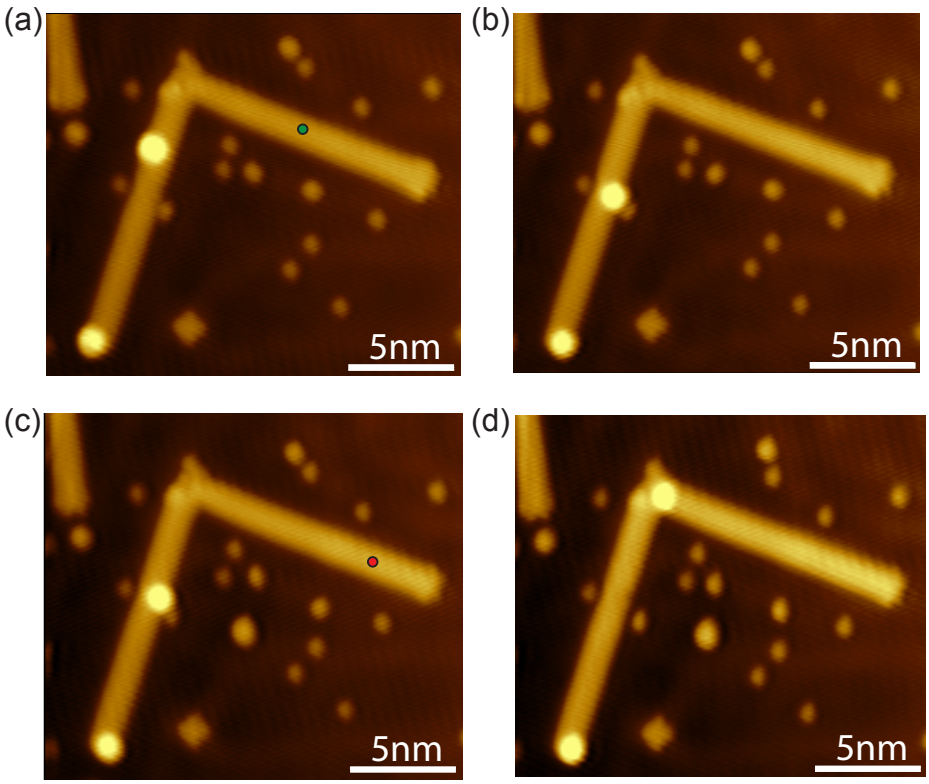

Figure 2.18: **Motion of a Co adatom on a GNR after voltage pulse around the corner of the GNR.** (**a**), (**b**) STM images before and after a positive voltage pulse of V_b = 900 mV at the green dot in (a), respectively. (**c**), (**d**) STM images before and after a negative voltage pulse of V_b = −1000 mV at red dot, respectively.

2.8.2. RESULTS

In total we performed around 900 voltage pulses on GNRs with the amplitude up to 1200 mV and −1000 mV for positive and negative bias voltages, respectively. Parameters recorded with each voltage pulse are the value of the bias voltage (V_b), the tunneling current (I), the initial tip-adatom distance (X, ranging from 2.5 nm to 21 nm) and the resulting displacement of the Co adatoms (L). X was measured from the tip position at the moment of the pulse to the center of the Co adatom at its initial position, while L was measured from the center of the Co adatom in its initial position to the adatom's center at its final position. If the Co adatom was not displaced, L was noted as 0 nm. Criteria for recording successful migration of adatoms were as follows:

- $|V_b| \geq |\pm 600|$ mV (voltage amplitudes lower than this value did not result in a significant fraction of moved Co adatoms)
- $|I| \geq |\pm 0.3|$ μA (this value was recorded as the tip−GNR point contact current for ±100 mV bias voltage)
- Co adatoms at the end points of GNR were not added to statistics as their motion was limited only to the direction towards the tip
- Co adatoms at the corner of kinked GNR were not added to statistics (we have not observed any displacement of these adatoms)
- Only observations for single Co adatoms were registered (clusters of two or more adatoms were dismissed)

Table 2.1 shows all events that occurred after voltage pulses. An event is considered as a motion of one Co adatom on the GNR on which the voltage pulse was performed, thus for one voltage pulse multiple adatoms might move, resulting in more than one event per pulse. Around half of the adatoms were displaced from their initial position

Cobalt on GNR	
Total number of events	1504
Number of Co that did not move	764 (50.8%)
Number of displaced Co (includes events below)	740 (49.2%)
- Co moved along GNR	543 (36.1%)
- Co moved left/right on GNR	55 (3.7%)
- missing Co	136 (9%)
- Co fell on Au(111)	6 (0.4%)

Table 2.1: **Statistics for migration of Co adatoms on GNRs after voltage pulses.** Total number of voltage pulses is around 900.

after the pulse. Displaced adatoms include the ones that moved along GNR, the ones that moved laterally ("left/right"), the ones that fell on gold substrate and the ones that were removed from GNR and were not traced back (so-called *missing* adatoms). Subsequent scans of the area around GNR in order to locate the missing Co adatoms showed that only in a few cases Co dropped on the gold surface (always in the vicinity of the initial Co position on the GNR).

ESCAPE PROBABILITY

In Figure 2.19(a) we show the escape probability of Co adatoms on GNR after a voltage pulse, as a function of the initial tip-adatom distance (X). By the escape probability we mean the probability for the Co atom to escape from the local potential well in which it is initially residing. Experimentally this is defined as the ratio of the number of displaced adatoms on a GNR and the total number of adatoms on the GNR at initial distance X:

$$\Gamma = \frac{N_{\text{displaced}}}{N_{\text{total}}} \quad , \quad \Delta\Gamma = \sqrt{\frac{\Gamma(1-\Gamma)}{N_{\text{total}}}}. \tag{2.5}$$

The second expression in 2.5 gives a measure of the statistical accuracy of the escape probability. Each data point in Figure 2.19 corresponds to a 2 nm wide range of X values. For example, the value of X = 3 nm corresponds to 2 nm ≤ X < 4 nm range of values; the value of X = 5 nm corresponds to the range of values 4 nm ≤ X < 6 nm, and so forth. The number $N_{\text{displaced}}$ includes all events for which the atoms have left its initial position, including those where the atoms have disappeared from the GNR. With the exception of the first few data points which appear to have nearly the same

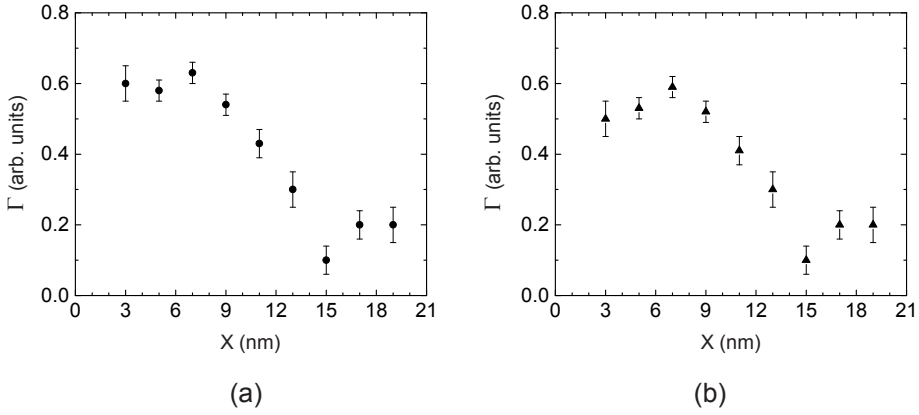

Figure 2.19: **Escape probability Γ as a function of initial tip-adatom distance.** (**a**) Γ(X) for all events. (**b**) Γ(X) for events excluding missing Co adatoms. Each X represents a 2 nm wide range of data points.

value, we observe a drop of the escape probability over the length scale of ~ 12 nm.

Figure 2.19(b) shows the escape probability for Co adatoms, excluding the missing Co adatoms. We observe a similar trend, with the escape probability for each X slightly lower than the one in panel (a).

The first four data points (X ≤ 10 nm) in both graphs in Figure 2.19(a) have similar values for the escape probability, and we observe a drop with increasing X beyond 10 nm and a leveling off beyond 15 nm. If we take the escape probability to be constant for X ≤ 10 nm, then we can group the data together for this range of X and we can plot the escape probability (β) as a function of the height of the voltage pulse for both subsets of the data, where β is defined analogous to Γ in Eq. 2.5. The difference in symbols emphasizes the fact that the two quantities refer to different selection criteria from the data sets. In Γ we have grouped up all voltage pulse heights together, in β we have lumped all $X \leq 10$ nm together. Figure 2.20(a), (b) shows β(V) for all events and for events excluding missing adatoms, respectively. The data is fitted to an exponential function $\beta = e^{-\frac{c}{\sqrt{V}}}$ where c is a fitting parameter [67]. The red and green curves are fits to negative and positive voltage data points, respectively, showing that the two data sets are fairly symmetric in voltage. We also obtained partial data for lower voltages (e.g. ±500 mV), however we do not have enough statistics to present it.

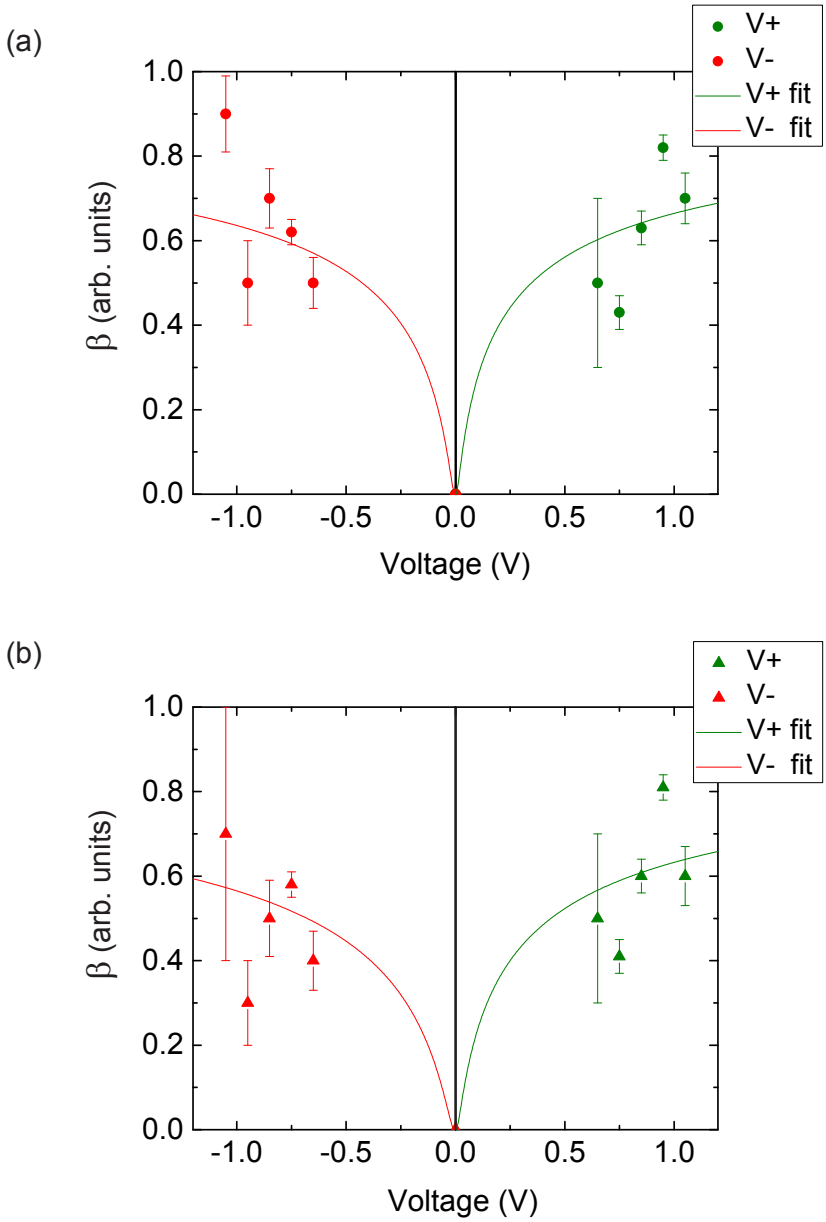

Figure 2.20: **Escape probability β as a function of voltage for X ≤ 10 nm.** (**a**) β(X) for all events. (**b**) β(X) for events excluding missing Co adatoms. Red and green lines represent exponential fits for negative and positive voltage, respectively.

VOLTAGE - DISTANCE CHARACTERISTICS

The length of displacement of Co adatoms on the GNR (L) for all voltage pulses V is plotted in Figure 2.21, where green and red dots indicate positive and negative voltage, respectively. Obviously, adatoms that went missing or that dropped onto the Au(111) surface are not included in this plot. Positive L values indicate motion of Co adatoms away from the tip while negative values indicate motion towards the tip. Voltage pulses that did not induce motion of adatoms (L = 0) were not included in the graph for clarity (and they are also not included in the statistical averages). The average value of L for positive voltage pulses is $L+ = 0.2 \pm 0.2$ nm, whereas the average value of L for negative voltage pulses is $L- = 0.1\ ^{+0.2}_{-0.1}$ nm. Both values are close to zero, indicating undetectable directional motion. In order to analyze whether L can be affected by the initial tip-adatom distance X, we also plotted the displacement L for different voltage pulses, separately for small X (≤ 10nm) and for large X (> 10 nm), Figure 2.22(a), (b) respectively. The average displacement for small X is $L-_S = 0.3 \pm 0.3$ nm and $L+_S = 0.2 \pm 0.2$ nm. Large X gives average values of $L-_L = -0.4 \pm 0.2$ nm and $L+_L = 0.1\ ^{+0.2}_{-0.1}$ nm. Again the values that we obtained are quite small, suggesting that

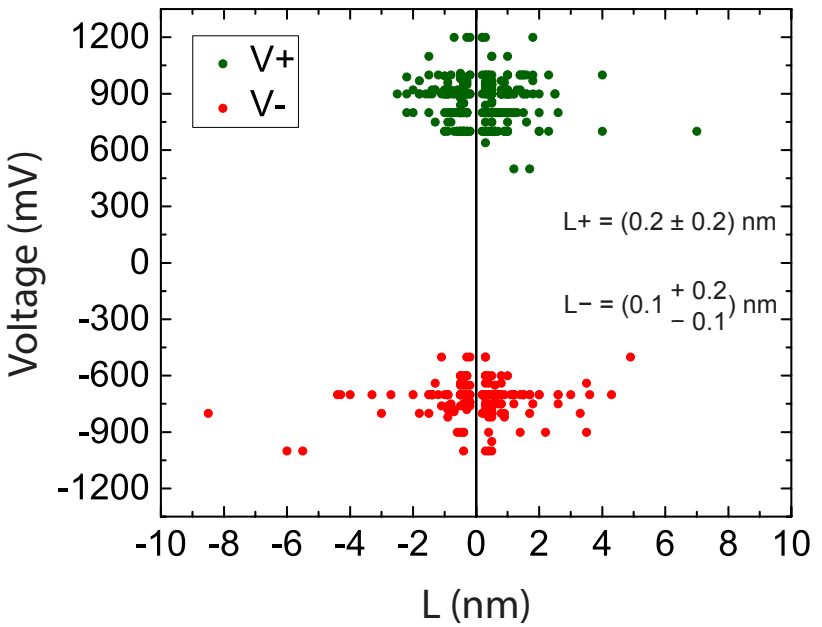

Figure 2.21: **Displacement of Co adatoms (L) after a voltage pulse V.** L+ and L- note average values of L for positive and negative voltage pulses, respectively.

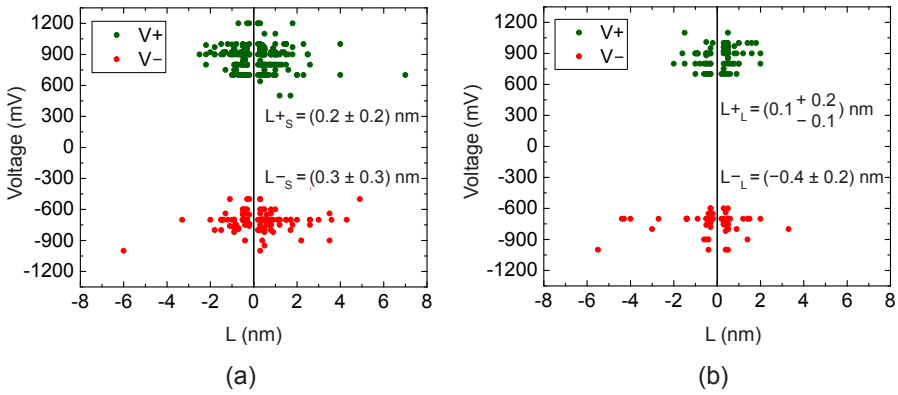

Figure 2.22: **Displacement of Co adatoms after voltage pulse V. (a)** L for X ≤ 10 nm. **(b)** L for X > 10 nm. L+ and L- note average values of L for positive and negative voltage pulses, respectively.

even if there is directional motion, the magnitude is at the border of our experimental resolution.

Figure 2.23 shows a histogram of the distance L traveled by adatoms after the voltage pulse, including the events for which no displacement was detected (L = 0). Maximum observed values for L are −8.4 nm and 7.1 nm. The green line is a fit of the right-hand side data (positive L), excluding L = 0, to the 1-dimensional [6] random walk probability distribution P [68], with the hopping rate (ν_p) and a prefactor (A_p) as fitting parameters. The fit is extrapolated to L = 0 and mirrored to the left side. P is obtained by considering the probability for an atom to jump to the nearest-neighbor sites [7] along a straight line (see Appendix for more details). The red line is the equivalent fit to the negative L data set, with ν_n and A_n as fitting parameters. Initial fitting with only the hopping rate as fitting parameter did not yield a good fit of both the L = 0 bar and the tails of the distribution. Introducing a prefactor lowers the total probability from 1 to the value of A and ensures a good fit to all the data points except for L = 0. This will be discussed later in the chapter.

After several hundreds of pulses we observed that Co adatoms are removed from the GNR more often after negative voltage pulses compared to the positive ones of the same amplitude. Table 2.2 shows statistics for these missing Co adatoms after positive and negative voltage pulses. One can see that even for the lower average voltage amplitude (V_{avg}) and larger average initial tip-adatom distance (X_{avg}), the fraction of missing adatoms for negative bias voltage is more than two times larger

[6] Even though GNRs are 2-dimensional, in the first approximation it suffices to use this model

[7] A better fit of the theoretical probability distribution to the experimental data is obtained if the next-nearest-neighbor jumps are also taken into account [68, 69], however this single jumps approximation is adequate for a first approximation required in this analysis

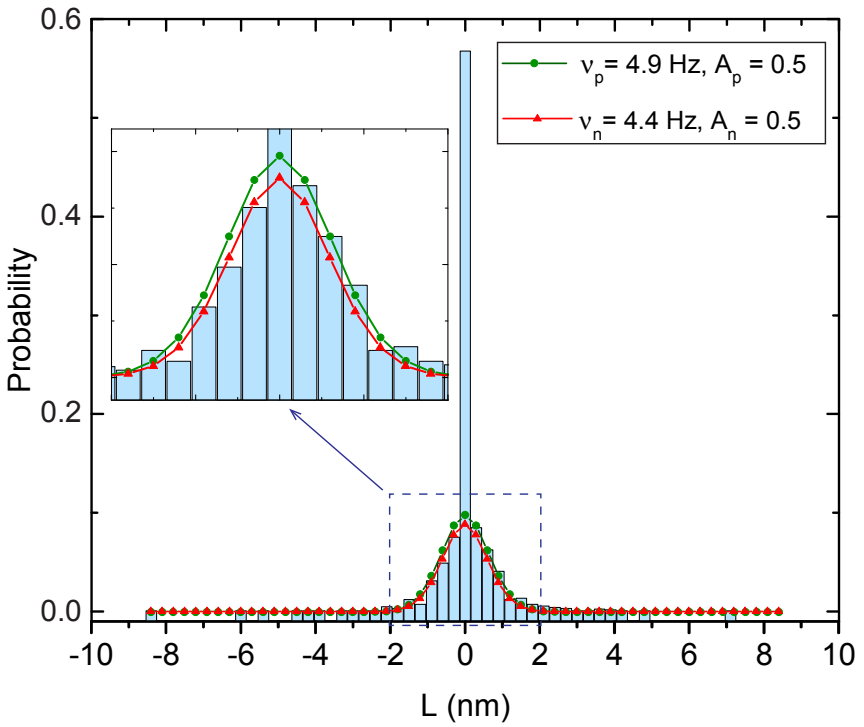

Figure 2.23: **Histogram of the distance traveled by Co adatoms along GNR after a voltage pulse (t ~ 0.5 sec).** Positive (negative) L indicates motion away from (towards) the tip, while L = 0 nm indicates Co adatoms that did not move. Green line is the fit of the positive L data to the 1-dimensional random walk probability distribution, excluding the data points for L = 0. Fit is extrapolated to L = 0 and mirrored to the left side. Fitting parameters are the hopping rate ν_p, (4.9 ± 0.4) Hz and a prefactor A_p, (0.5 ± 0.3). (see Appendix for details). Red line is the equivalent fit of the negative L values mirrored to the right side, with fitting parameters ν_n = (4.4 ± 0.4) Hz and a prefactor A_n, (0.5 ± 0.3). The inset shows zoom-in on the small area in a dashed box.

than for the positive one. This is one of the reasons why we limited the amplitude of negative voltage pulses to -1000 mV.

Positive voltage			**Negative voltage**		
Missing Co	$V+_{avg}$	$X+_{avg}$	Missing Co	$V-_{avg}$	$X-_{avg}$
9%	886 mV	7.3 nm	**21**%	-733 mV	8.2 nm

Table 2.2: **Statistics for missing Co adatoms for positive and negative voltage pulses.** $V+_{avg}$ and $X+_{avg}$ are the average voltage amplitude and initial tip-adatom distance for positive voltage pulses, while $V-_{avg}$ and $X-_{avg}$ correspond to negative voltage pulses.

COBALT ADATOMS ON AU(111)

During voltage pulses on GNR we have sometimes observed motion of Co on Au(111) close to the GNR. Figure 2.24 shows an image scan before (a) and after (b) a voltage pulse of 800 mV on the GNR (green dot). It can be seen that a Co adatom on Au(111) close to GNR (yellow arrow) moves towards the GNR after the pulse.

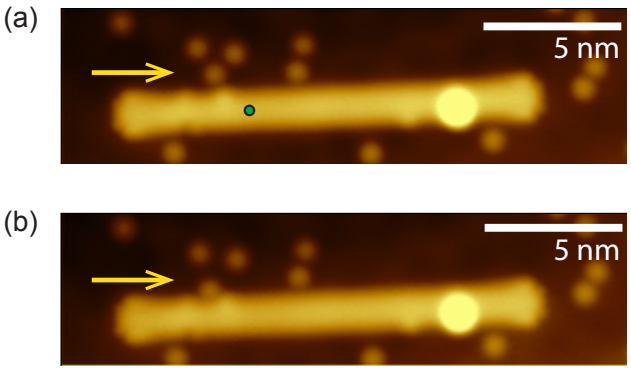

Figure 2.24: **Motion of Co on Au(111).** STM images before (**a**) and after (**b**) a voltage pulse of V = 800 mV on a GNR. The green dot indicates the place of the pulse. The yellow arrow points at the Co adatom on Au(111) that moved.

We have obtained statistics for voltage pulses on the GNR that moved Co adatoms on Au(111) within a range of 7 nm radius from the place of the pulse (first row in Table 2.3). This range was selected because it covers an area that is visible in most of the scans taken.

In order to make a quantitative comparison, we performed voltage pulses on gold to induce migration of Co adatoms on gold. We used the same procedure of lowering the tip and the same initial parameters as for Co on GNR ($|I| \geq |\pm 0.3|$ μA, V_b = 100 mV) and we applied voltage pulses in the range of -1000 mV $\leq V_b \leq -600$ mV and 600 mV $\leq V_b \leq$ 1200 mV. Here we also take into account only Co adatoms on gold

Event	Displaced Co
Displacement of Co on Au(111) after pulse on GNR	391 / 6331 (6%)
Displacement of Co on Au(111) after pulse on Au(111)	16 / 519 (3%)
Displacement of Co on GNR after pulse on GNR	740 / 1504 (49%)

Table 2.3: **Overview of different pulsing events.** First number in the right column is the number of displaced Co adatoms and second number is the number of all Co adatoms in the area of interest. Last row corresponds to the statistics for Co on GNR from Table 2.1.

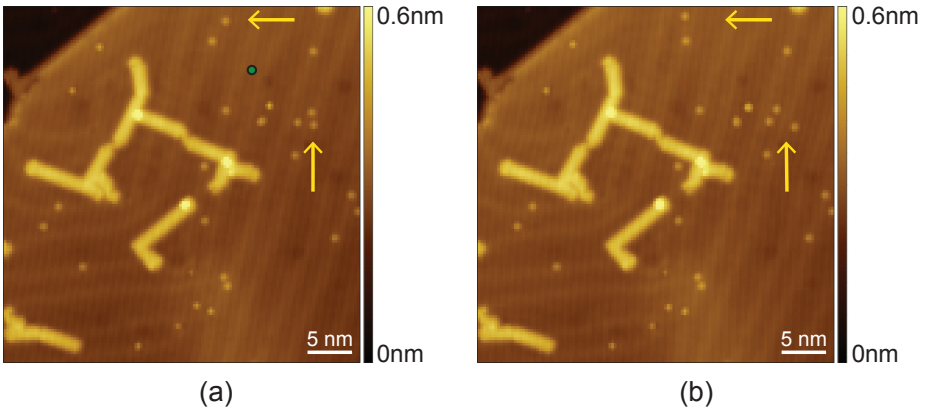

Figure 2.25: **Manipulation of Co adatoms on Au(111).** STM images (**a**) before and (**b**) after a voltage pulse of 1200 mV (green dot). The area taken into account in the analysis is a circle of 7 nm radius from the green dot. The yellow arrows point at three Co adatoms that moved, and also serve as a reference marking the same position in both images.

that were within the 7 nm radius from the place of the pulse. Figure 2.25 shows STM images before (a) and after (b) a voltage pulse of 1200 mV applied at the position of the green dot. We can observe motion of several adatoms around the place of the pulse (two yellow arrows point at three Co adatoms that moved after the pulse). Obtained statistics for these events is shown in the second row of Table 2.3. Compared to migration of Co on GNR, the statistics shows that current-induced migration of Co adatoms on GNR (third row of Table 2.3) is much more effective than moving Co on Au(111). It also shows that motion of Co on Au(111) is nearly equally (in)effective for pulsing on GNR and Au(111).

We also observed that sometimes Co on Au(111) far away from the place of the pulse, but in the vicinity of the GNR, moves after voltage pulses on the GNR. Figure 2.26(a), (b) shows an example of such motion (the green dot marks the position of the tip during the pulse of 700 mV). We did not do an extensive quantitative analysis of these events (as mentioned before, they are not added to the statistics because the distance is larger than 7 nm).

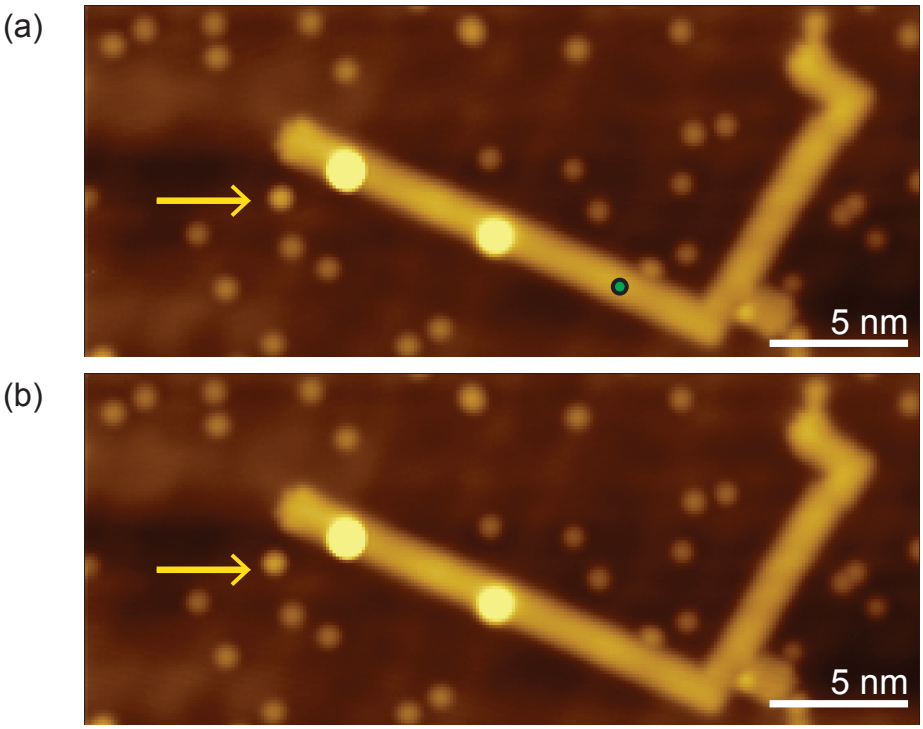

Figure 2.26: **Motion of Co on Au(111) in the vicinity of the GNR.** STM image before (**a**) and after (**b**) a voltage pulse of 700 mV (green spot). The yellow arrow points at Co adatom that moved, and also serves as a reference marking the same position in both images.

2.8.3. TEMPERATURE-DEPENDENT DIFFUSION MEASUREMENTS

In order to obtain more information on the relative excitation energies of Co adatoms on GNR and on Au(111), we performed a series of temperature-dependent diffusion measurements. Temperatures higher than 10 K were achieved by slowly heating the entire STM scan head, which is thermally weakly coupled to the helium bath. As temperature sensor we used a DT-470 diode sensor (Lake Shore Cryotronics) attached to the scan head. For our diffusion study, sequences of STM images were recorded at different temperatures. The temperature was raised from 8 K in steps of ~ 15 K up to 79 K. For each step we waited several hours to reach thermal equilibration before starting the acquisition of image sequences. Co adatoms on Au(111) were already diffusing at 34 K. Figure 2.27 shows two STM images obtained at 46 K, where (a) is acquired 7 min before (b). Motion of a Co adatom on Au(111) is noticeable as the adatom is moved from its initial position (indicated by the yellow arrow), while the Co adatoms on the GNR remain unaffected.

Figure 2.27(a) confirms a well-known observation that adatoms prefer to sit at the corners of the herringbone. In other words, not all positions on Au(111) are equal, some lattice sites have a deeper energy well and are preferentially occupied [70]. We also observed that there are some sites on GNR from which it is very hard to remove Co adatoms. This could be due to the interaction of Co with adsorbates or with the herringbone reconstruction on gold below. Also as mentioned before, there is at least one type of such pinning site, which is a corner of a GNR which creates a stable position for Co adatom. This means that the escape probability may depend on the

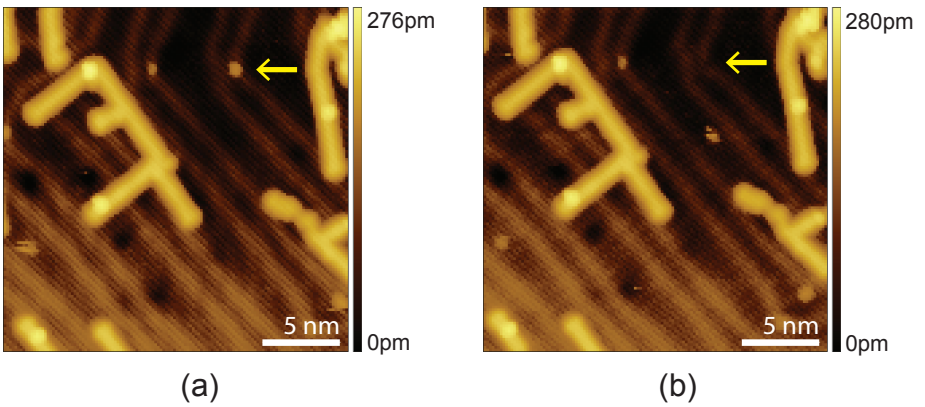

Figure 2.27: **Temperature-dependent diffusion measurement.** (**a**) STM image of the sample at 46 K. (**b**) STM image of the same area at the same temperature obtained 7 min after (a). The yellow arrow points at a Co adatom that moved, and also serves as a reference marking the same position in both images. The scan area is slightly shifted due to thermal drift. V_b = 0.1 V, I = 1 pA

initial positions of Co adatoms.

When 79 K was reached, the time required for the temperature to stabilize became very long, and we did not increase the temperature any further. Even at 79 K motion of Co on GNR was not observed, while most of the single Co on Au(111) could not be seen any longer (they either grouped up into clusters or possibly jumped towards the tip during scanning). Figure 2.28 shows an exemplary case of displacements of Co on Au(111) at 34 K, where L = 0 corresponds to Co adatoms that did not move. Each L corresponds to a 0.3 nm wide set of values (e.g. L = 0.6 nm takes all values from 0.45 to 0.75 nm). Yellow bars show the experimental probability distribution, while brown bars show the fit of a 2-D random walk on a triangular grid to the experimental data, with the hopping rate ν as a fitting parameter (see Appendix for details). The fit gives the value of ν = 0.025 Hz.

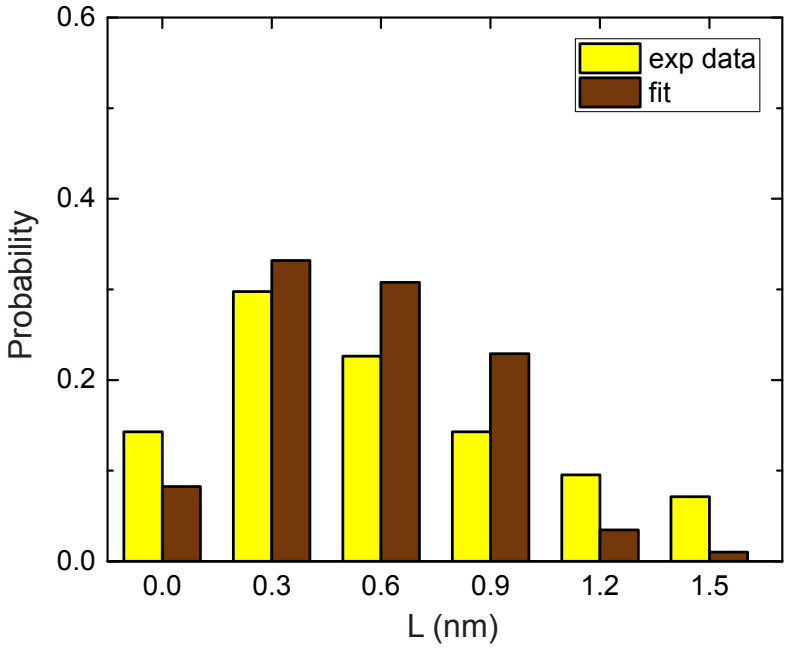

Figure 2.28: **Comparison of the 2-D random walk (brown) and experimentally observed (yellow) probability distribution for displacement of Co (L) on a triangular lattice of Au(111) at T = 34 K.** The values L = 0 nm indicate Co adatoms that did not move. The calculated distribution corresponds to a hopping rate of ν = 0.025 Hz.

2.9. DISCUSSION

There are two mechanisms involved in the motion of adatoms after voltage pulses: Joule heating which results in a stochastic motion, and current-induced forces which, with the help of Joule heating needed to excite an atom out of its equilibrium position, would give preferred direction of motion. Figure 2.29 shows a schematic diagram of the path that the current (carrying a part of the heat) presumably takes after a voltage pulse from the STM tip. Thicker red arrows indicate higher current density. A large part of the current goes straight from the place of the pulse to bulk of gold. The remaining part of the current most likely spreads evenly along the GNR and seeps into the bulk of gold. When hot electrons are injected with the STM tip, there is a certain distance over which they will travel before thermalizing and the area within this radius will become equally hot. This area is represented with a red semicircle, with a center at the tip position on GNR and a radius of the mean free path (MFP) of the injected hot electrons and induced phonons in the GNR. In order to estimate the contribution of each mechanism (heat and current-induced forces), we need to look for evidence of directional motion of Co adatoms due to the part of the current flowing along the GNR.

We now turn to our experimental results. The first thing that we notice is that Co adatoms stay on GNRs after pulsing with the STM tip (only 0.4% of events showed adatoms to have dropped on gold). This suggests the presence of a potential barrier at the edges of GNRs which is much higher than the barrier for leaving the initial site. GNRs, therefore, provide a path for one-dimensional diffusion of Co adatoms.

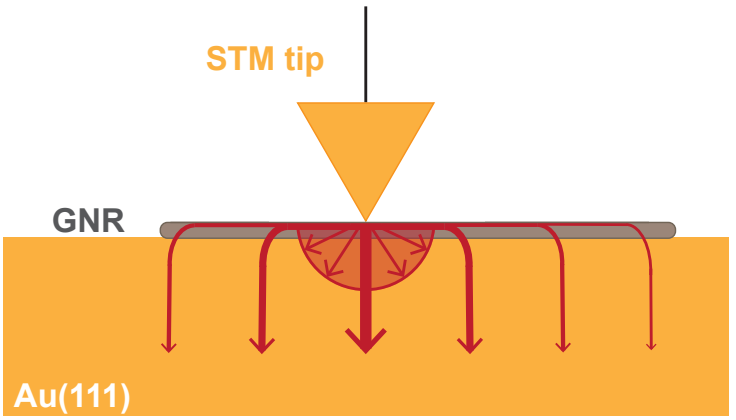

Figure 2.29: **Schematic diagram of the current flow.** The red arrows indicate split current paths from the STM tip during a voltage pulse. The red semicircle represents a hot spot around the place of the pulse. Thicker red arrows indicate higher current density.

From Figure 2.19(a) and (b) (which shows Γ(X) for all events and events excluding missing Co, respectively) we see that the first four data points (for $X \leq 10$ nm) have similar values. When we consider the atoms as sitting in potential wells of depth E_D, the probability of escaping from this well should be determined by the local effective temperature. The constant level of Γ for the first few data points therefore points at a nearly constant temperature in this region. This suggests that the radius of the hot spot around the place of the pulse is ~10 nm (which is presumably equivalent to the MFP of the injected electrons and induced phonons). Although still inside the accuracy margin, one may recognize a slight trend of the first three data points in Figure 2.19(b), which seems counter-intuitive: the escape probability for the larger X is higher than the one for the smaller X. This is actually consistent with the assumption that Co adatoms closest to the tip (i.e. smallest X) are more likely to jump to the tip after a voltage pulse and disappear from the statistics. Since this graph does not show missing Co adatoms, this trend is to be expected. For $X > 10$ nm, Γ decays by a factor of ~3 over the distance of around 12 nm. This indicates the presence of a thermal gradient along the GNR with a hot spot around the place of the pulse and colder spots towards the ends of the GNR. It also implies that GNRs are in a close contact with gold surface: if they were isolated, the temperature of GNRs would be constant along their entire lengths, and in turn Γ would also be constant.

The fits to the escape probability β for positive and negative voltages in Figure 2.20 (green and red curves, respectively) show that the escape probabilities are symmetric for positive and negative bias voltage. In addition, average values for L obtained from the V(L) distribution (Figure 2.21) are the same, within experimental accuracy, for both voltage polarities, which indicates an overall lack of directionality of Co motion. The same conclusion can be drawn from the distribution for small X (Figure 2.22(a)) and the equal values obtained for $L+_S$ and $L-_S$. The distribution for large X (Figure 2.22(b)) shows a slight directionality of Co motion towards the tip for V−, however it is quite small ($L-_L$ = - 0.4 ± 0.2 nm). The symmetric distribution of diffusion in both directions is further confirmed by the red and green fits in Figure 2.23, which shows that the distributions left and right of L = 0 are symmetric, to within experimental accuracy. In order to estimate whether preferred directionality of Co motion is expected for the range of voltages we used in the experiments, we need information on the GNR conductance and density of states which will tell us whether we are probing the electronic states of GNR or the surface states of the underlying gold.

2.9.1. GNR CONDUCTANCE

Grill *et al.* [60] calculated the conductance of a 7-AGNR, lifted off the surface of gold with the STM tip (Figure 2.30). Quite different slopes are obtained for high and low bias voltages. For low bias voltage of −0.5 V (below the HOMO level) the conductance drops nearly exponentially with the effective GNR length spanning the junc-

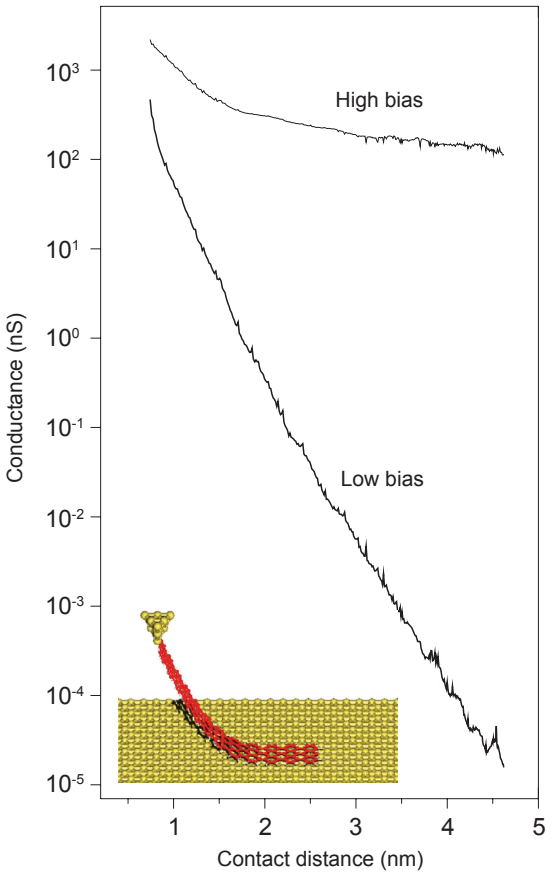

Figure 2.30: **Calculated conductance of a 5 nm AGNR in an STM pulling configuration as a function of effective molecular length in the junction.** Low bias = −0.5 V (in the gap); high bias = −1.2 V (matching HOMO level)). The high bias curve first decays (up to a contact distance of 1.5 nm) and then remains almost constant at larger contact distances. Image taken with permission from [60].

tion. Such a low conductance at small bias voltages is explained by the lack of overlap of two Tamm states[8] located at the opposite GNR termini, so they do not contribute to the conductance. For high (absolute) bias voltage of −1.2 V (probing the HOMO level) the curve first decays (up to a contact distance of 1.5 nm), because the Tamm state contribution is captured at this stage, and then it stays almost constant at larger contact distances.

Fasel *et al.* [71] compared dI/dV spectra of an armchair GNR with N = 7 (7-AGNR) on an insulating gold silicide monolayer (AuSIL) to the one on Au(111). The differential conductance dI/dV signal is obtained by positioning the tip of a scanning

[8] Tamm states are present close to the Fermi level at around 30 meV [60]

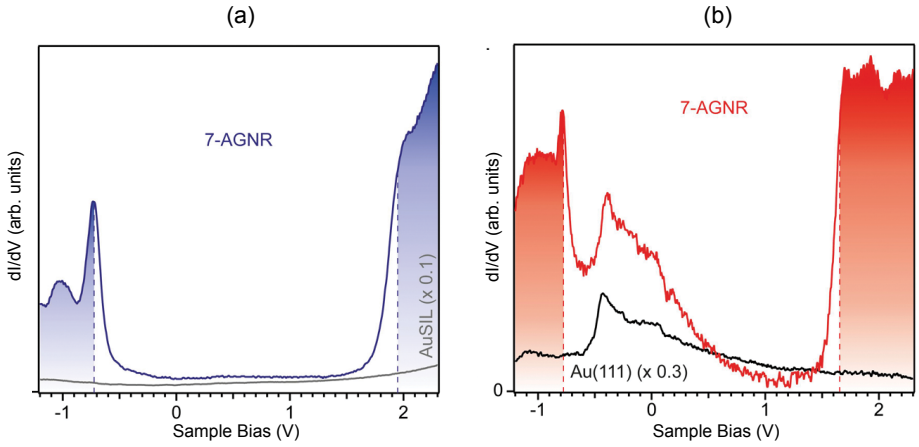

Figure 2.31: **Comparison of differential conductance spectra of 7-AGNR on an insulator and a metal** [71]**.** (**a**) dI/dV spectrum of a 7-AGNR on an insulating gold silicide (AuSIL). (**b**) dI/dV spectrum of a 7-AGNR on Au(111) substrate. The GNR spectrum is dominated by the Au(111) surface state. Image reproduced from [71] with permission.

tunneling microscope (STM) above the middle of the GNR and setting the tunneling gap to the desired value. The feedback loop is opened to allow the current to vary and the bias voltage is ramped from -1.5 V to 2.3 V. The dI/dV signal is directly proportional to the local density of states (LDOS) of the sample at the position of the tip. Depending on the sign of applied bias, the occupied or the unoccupied states are probed. The *dI/dV* signal is recorded directly using an external lock-in amplifier. A small sinusoidal voltage modulation is added to the bias voltage, causing a sinusoidal response in the tunneling current. The amplitude of the modulated current is sensitive to the slope of the *I*-*V* curve (hence, a dI/dV signal). The *dI/dV* signal is convoluted with the DOS of the tip, which is not constant. The results will vary from tip to tip, and the tip may even change in between STS measurements.

Due to suppression of Au(111) surface state by the silicide top layer, dI/dV spectra of 7−AGNR on AuSIL exhibit a featureless band gap region[9] (Figure 2.31(a)). Well-defined peaks at −0.7 eV and 2 eV correspond to the valence band maximum and conduction band minimum, respectively. 7−AGNRs on Au(111) are dominated by the metal's surface state, which slowly decays into the vacuum in comparison to some GNR states that are found only in the vicinity of the ribbon [65]. As a result, the rapidly decaying GNR states might be obscured by substrate contribution in an STS measurement [72]. The most prominent contribution stems from Au(111) surface states with an onset at around −0.4 V, as can be seen on Figure 2.31(b). For 7−AGNR on Au(111) the valence band maximum is at −0.8 eV and the conduction band minimum is at 1.6 eV, resulting in a band gap of 2.4 eV.

[9] Even though it is referred to as gap, dI/dV is nonzero between HOMO and LUMO levels

From this we infer that for the range of positive bias voltages used in experiments ((0.6 - 1.2) V) the GNR behaves as a semiconductor (low conductance regime), whereas for negative bias voltages (-(0.6 - 1) V) electrons are injected into the HOMO level of the GNR and the behavior is expected to be metallic (we are in a high conductance regime, probing the HOMO level). We can now estimate the distribution of the current after a voltage pulse: for V+ the current will mostly flow directly to the bulk of gold and we should not expect to see directional motion, whereas for V− the current will partially flow along the GNR and we could expect to see directionality towards the tip due to a current-induced wind force.

Even though we do observe a slight asymmetry in distribution for V- for large X, it is not statistically significant and we cannot identify current-induced forces from our measurements. We, therefore, conclude that migration of Co adatoms on GNR occurs mainly due to heating of the GNR. The GNR will be heated by the current, and this heat is carried away to the bulk of the Au substrate through the electrons and through lattice vibrations. Anticipating that there is an electronic and phononic barrier for this heat transport, the GNR will act as a line source of heat. We have observed motion of Co on Au(111) in the vicinity of the GNR far away from the voltage pulse on the GNR (Figure 2.26), which confirms efficient thermal transport along GNR. The reason why we do not observe significant directional motion of Co is likely due to the insufficient current density injected into the GNR.

It is worth mentioning that Lee *et al.* [73] in their recent paper demonstrate another source of asymmetry by which the electronic transmission characteristics of atomic-scale junctions are related to their heat dissipation properties. They show that depending on whether the molecule in the junction has electron- or hole-dominated electrical transport, the heat dissipation in the sample will be smaller (larger) for V- than V+. However, the difference in temperature increase for the two bias polarities is quite small (the order of a few mK) and would not be detectable in our system.

2.9.2. HOPPING RATE AND DIFFUSION BARRIER

The extrapolated fits of the one-dimensional random walk probability to positive and negative L data sets separately (Figure 2.23, green and red line, respectively) give values for the hopping rates of $\nu_p = (4.9 \pm 0.4)$ Hz and $\nu_n = (4.4 \pm 0.4)$ Hz. The values of the hopping rates are the same within the error, which further confirms that the motion is almost equally probable in both directions and that there is no detectable directional motion.

Around 50% of the voltage pulses did not result in the displacement of Co adatoms (L = 0). There are several possible reasons for this. The first one is the stochastic (probabilistic) nature of hopping which implies that some of the adatoms will not always escape from the potential well after sufficient amount of energy is injected. Another reason is that during a voltage pulse Co adatom could hop away and back

to its initial position. The third possible reason is a deeper potential well of certain spots in which Co resides, which mean that our underlying assumption of a uniform potential well depth is invalid. As mentioned in the subsection 2.8.3, Co adatoms have preferred lattice sites on Au(111) (such as the corners of the herringbone). It is possible that similar preferred spots exist on GNR as well. One such example is the bend of the GNR from which it was not possible to move Co. The fit of the experimental data to a 1-D random walk function (Figure 2.23) gives us the information on these special sites. Since we found that we were forced to introduce the fitting prefactors in a 1-D random walk function ($A_p = 0.5 \pm 0.3$, $A_n = 0.5 \pm 0.3$) in order to have a good fit of the values for L $\neq$ 0, the total integrated probability is then 50% (instead of 100%). The fact that the experimental value for L = 0 is much higher than the fit value is a clear sign that there are exceptional sites on GNR with deeper energy wells from which adatoms are harder to move.

We can now obtain an estimate for a lower limit of the diffusion barrier for Co on GNR. The hopping rate ν is given by

$$\nu = \nu_0 e^{-E_D/k_b T} \tag{2.6}$$

where ν_0 is the attempt frequency (typically an atomic vibration frequency of the order of 10^{12} Hz), E_D is the diffusion barrier, k_b is Boltzmann constant and T is temperature. In the thermal diffusion experiment, at T = 79 K we observe no motion of Co on GNR, which means that at this temperature the number of hops is less than one per image-to-image time interval of t = 180 sec. If we take the number of hops to be ~ 0.5, we obtain the minimum of the diffusion barrier $E_D \geq 0.2$ eV for Co adatoms on GNR [10]. Using this value of the lower limit of diffusion barrier, and the value for the hopping rate for Co on GNR obtained from the fitting (ν_p or ν_n), we estimate the lower limit for temperature of GNR during the voltage pulse to be $T_{min} = 90$ K.

2.9.3. VERTICAL CO DISPLACEMENT

The statistics from Table 2.1 shows that in 9% of the cases Co adatoms were removed from the GNR ("missing" adatoms). We attribute these events to vertical displacement of Co adatoms towards the tip, rather than lateral motion along the GNR. The reason for this is that the largest potential drop is between the tip and the sample, so the electric field lines are oriented mostly perpendicular to the surface of GNR.

Vertical motion includes two mechanisms: excitation of vertical vibrations of the adatom and forces that attract the adatom towards the tip (direct force or Van der Waals forces). Since we have similar heating effect for V+ and V− (Figure 2.20), this means that the electric field plays a key role in removing Co adatoms from the GNR.

The statistics from Table 2.2 shows that for missing Co adatoms there is asymmetry between V+ and V−. One possibility for the asymmetry could be the higher

[10] By comparison, theoretical value for Co on pristine monolayer graphene obtained by DFT calculations is 0.76 - 1.32 eV, depending on the adsorption site [74]

work function of the sample with respect to the tip (discussed in section 2.4). Since the work function of the sample is 500 meV higher than the one of the tip, there is an additional attractive force between the sample and the tip due to the equilibration of the chemical potentials. This means that the effective field is smaller for positive bias (where the applied filed helps to reduce the Kelvin potential) then for negative bias where it adds to it. As a consequence, adatoms would move easier towards the tip for V−.

2.9.4. ATOM AS A LOCAL THERMOMETER?

It is well known that diffusion of matter in a thermal gradient is directed away from hot spots and towards cold spots. Would it be possible to use single atom diffusion to detect temperature variations on the atomic scale? Theoretical work of Meair *et al.* [75] suggests that this could be a possibility: occupation of a hot spot by a single adatom should always lead to further adatom diffusion towards colder spots. This asymmetry in diffusion would in principle permit detecting temperature variations on the atomic scale, which could arise in structures such as the one in our experiment.

We concluded from Figure 2.19 that the hot spot on the GNR has a radius of ~10 nm and the temperature drops with further increase of X. Based on diffusion in a thermal gradient, we would expect a directional component for $X > 10$ nm. If the theory is applicable to our experiment, Co adatom in this range of X should always move towards the cold spots after the pulse, i.e. away from the tip. The statistics shows, however, that this is not the case, as L_{avg} for this data set has a value of $0.1\ ^{+0.2}_{-0.1}$ nm. If we want to observe the effect of thermal diffusion in a thermal gradient, a Co adatom has to make many hops. The first hop at a certain spot is still a random forward-backward motion even in a thermal gradient. It is only after many hops that one can effectively see a directionality in motion. The reason that we do not observe this directionality is that we have a global temperature gradient of a short duration (coming from a short voltage pulse) rather than a steady state in which the adatom has time to move away from hot spots. This suggests that the displacements of Co adatoms that we observe are mostly due to single hops or a few shorter hops within the short time of the voltage pulse.

2.9.5. CO ON AU(111)

The statistics from Table 2.3 indicates that the induced migration of Co on GNR (row 3) is much more efficient than migration of Co on Au(111) (rows 1, 2), despite the fact that we find that the potential wells for Co on GNR are deeper than for Co on Au(111). In addition, comparison between rows 1 and 2 indicates that migration of Co on Au(111) was equally difficult whether the pulsing was done on GNR or Au.

The most likely explanation for the difficulty of moving Co on Au(111) lies in the

current and heat distribution (Figure 2.32). When we apply a voltage pulse on gold (top-left black dot), the electric and thermal transport are limited to the vicinity of the place of the pulse (indicated by round yellow shade) due to the ballistic electron transport through the bulk of gold, without affecting much nearby Co adatoms (local distribution). Also the heat is carried away mostly by the electrons, which is a process that is fast compared to the relaxation of the GNR where the most efficient heat transport is along the GNR (indicated by the color gradient along the GNR, where red color represents a hot spot of ~10 nm radius). Rows 1 and 2 of the Table 2.3 suggest that the effect of pulsing on the GNR is very similar to pulsing on Au(111) when it comes to moving Co on Au(111). This implies that pulses on Au and on the GNR both lead to a local hot spot within a similar range over the Au surface (yellow shades; the dashed circle is for size comparison). Seeing how Co on Au(111) starts diffusing at around 34 K while Co on GNR does not move even at 79 K, we conclude that diffusion barrier for Co on Au(111) is much smaller that the one for Co on GNR. We also draw the conclusion that pulsing on the GNR heats the GNR to a much higher temperature than the Au surface, and that pulsing directly on gold leads to a similar modest local temperature rise of the Au surface as induced by pulsing on a GNR.

The diffusion barrier for Co on Au(111) is given by

$$E_d = -k_b T \ln\left(\frac{\nu}{\nu_0}\right) \tag{2.7}$$

where k_b is Boltzmann constant and $\nu_0 \sim 1$ THz = 10^{12} Hz. Using the average hopping rate $\nu = 0.025$ Hz obtained from the fit of a two-dimensional random walk probability to experimental data at T = 34 K, we obtained diffusion barrier for Co on gold $E_{D_g} = 0.092$ eV. By comparison, the diffusion barrier for Co adatoms on Cu(111) is 0.01 - 0.4 meV, depending on the adsorption site [76].

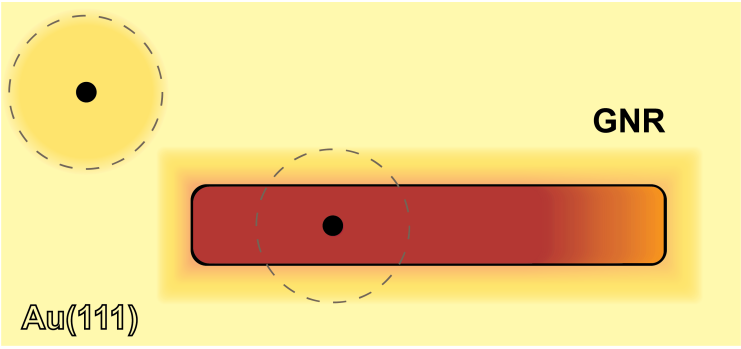

Figure 2.32: **Diagram of a heat distribution.** Black dots indicate place of the pulse on gold and GNR. Colors indicate different temperatures: yellow disc is temperature spread on gold and it is around the same size as the spread around GNR (dashed circle is for size comparison). Red color on GNR indicates the hot spot, with temperature gradually dropping with distance.

2.10. CONCLUSION & OUTLOOK

In summary, we have shown that it is possible to study one-dimensional migration of single Co adatoms on 7-AGNR on Au(111) by applying voltage pulses from an STM tip while in point-contact with GNRs. This experiment is the first step towards a detection of current-induced forces on a scale of single atoms. Interestingly, GNRs provide a lateral confinement due to the potential barrier at the edges, limiting the diffusion to be effectively one-dimensional, which makes the study of atomic diffusion a lot simpler. Although we inject electrons at negative bias polarity into the HOMO level of the GNR, analysis of escape probability and voltage-distance characteristics show no detectable directionality of Co migration which would come from current-induced forces. Slight directionality towards the tip for negative bias voltage is not significant enough to draw a definitive conclusion about detection of the wind force. The reason for this is most likely an insufficient current density along the length of the GNR. We infer that the observed motion of Co adatoms is mainly stochastic, under the influence of thermal excitations.

The statistics shows that it is much easier to move Co on GNRs than Co on Au(111). We attribute this to different current and heat distributions in the two substrates: voltage pulses on a GNR cause the entire GNR to become hot with a wide area of maximum temperature around the pulse, while on Au the heat is localized at the place of the pulse and quickly dissipated to the bulk. We have additionally performed temperature-dependent diffusion measurements in order to gain information on the relative energy barriers for Co adatoms on GNR and Au. Our findings suggest that there is a smaller relative barrier for Co on Au compared to the one on GNR, and that pulsing on GNR heats up the GNR to a much higher temperature than the Au surface, even when compared to pulsing directly on Au.

The experiment could be further improved by depositing GNR on a thin insulating layer (such as NaCl or hexagonal boron nitride), ideally with one end connected electrically to the substrate. This would confine the current within the whole GNR and also enable the GNR to stay hot for longer periods of time after the voltage pulse. Recent experiments have already demonstrated that it is possible to transfer a GNR from the metallic growth substrate onto insulating islands of NaCl, using the STM tip [77]. Going back to the initial experiments where we used CVD grown graphene, a possible improvement would be to decrease the width of the graphene patch to 30 μm, which would yield a 10 times higher current density for the same value of I_{max}. Using such a small sample would require a method of tip guiding [78] to avoid crashing the tip onto the insulating SiO_2 substrate. Regarding polymer contamination of graphene, an improvement would be to use a recently developed technique of graphene transfer in water, without using polymer [79], which would remove one polymer-deposition step. It should also be noted that SiO_2 has corrugated surface and Co adatoms sitting in the dips might be harder to move, thus switching to a more

flat insulating substrate (such as quartz) would help overcome this problem.

REFERENCES

[1] M. Gerardin. *Compt. Rend. Acad. Sci. Paris*, 53:727, 1861.

[2] W. B. Fiks. On the mechanism of the mobility of ions in metals. *Sov. Phys. Solid State*, 1:14–28, 1959.

[3] H. B. Huntington. Electromigration in metals, in: *Diffusion in Solids - Recent Developments*, A. S. Nowick and J. J. Burton (Eds.). *Academic Press, New York*, 51:303, 1975.

[4] C. Bosvieux and J. Friedel. . *J. Phys. Chem. Solids*, 23, 1962.

[5] R. S. Sorbello. Theory of electromigration, in: *Solid State Physics*, H. Ehrenreich and F. Spaepen (Eds.). 51, 1997.

[6] A. Christou. Electromigration and Electronic Device Degradation. 1994.

[7] R. E. Hummel. Electromigration and related failure mechanisms in integrated circuit interconnects. *International Materials Reviews*, 39:97–112, 2013.

[8] A. J. Learn. Effect of structure and processing on electromigration-induced failure in anodized aluminum. *Journal of Applied Physics*, 44:1251 – 1258, 1973.

[9] J. Cho and C. V. Thompson. Grain size dependence of electromigration-induced failures in narrow interconnects. *Appl. Phys. Lett.*, 54:2577 – 2579, 1989.

[10] M. J. Attardo and R. Rosenberg. Electromigration Damage in Aluminum Film Conductors. *Journal of Applied Physics*, 41:2381 – 2386, 1970.

[11] I. A. Blech and E. S. Meieran. Direct transmission electron microscope observation of electrotransport in aluminum thin films. *Appl. Phys. Lett.*, 11:263, 1967.

[12] J. C. Blair, P. B. Ghate, and C. T. Haywood. Electromigration-induced failures in aluminum film conductors. *Appl. Phys. Lett.*, 17:281, 1970.

[13] E. Arzt, O. Kraft, J. E. Sanchez, S. Bader, and W. D. Nix. Electromigration resistance and mechanical strength. *Mat. Res. Soc. Symp. Proc*, 239:677–682, 1992.

[14] I. A. Blech. Electromigration in thin aluminum films on titanium nitride. *J. Appl. Phys.*, 47:1203–1208, 1976.

[15] P. S. Ho and T. Kwok. Electromigration in metals. *Rep. Prog. Phys.*, 52:301–348, 1989.

[16] C. Y. Liu, C. Chen, and K. N. Tu. Electromigration in Sn-Pb solder strips as a function of alloy composition. *Journal of Applied Physics*, 88:5703 – 5709, 2000.

[17] S. Lin, Y. Liu, S. Chiu, Y. T. Liu, and H. Lee. Visualizing the Electron Scattering Force in Nanostructures. *Scientific Reports*, 7:3082, 2017.

[18] J. D. Verhoeven. Electrotransport as a means of purifying metals. *JOM*, 18:26–31, 1966.

[19] B. C. Regan, S. Aloni, R. O. Ritchie, U. Dahmen, and A. Zettl. Carbon nanotubes as nanoscale mass conveyors. *Nature*, 428:924–927, 2004.

[20] A. Barreiro, R. Rurali, E. R. Hernandez, and A. Bachtold. Structured Graphene Devices for Mass Transport. *Small*, 7:775 – 780, 2011.

[21] H. Park, A. Lim, and P. Alivisatos. Fabrication of metallic electrodes with nanometer separation by electromigration . *Applied Physics Lettres*, 75, 1999.

[22] W. Liang, M. Shores, M. Bockrath, J. Long, and H. Park. Kondo resonance in a single-molecule transistor. *Nature*, 417:725–729, 2002.

[23] H. Heersche, G. Lientschnig, K. O'Neill, H. van der Zant, and H. W. Zandbergen. In situ imaging of electromigration-induced nanogap formation by transmission electron microscopy. *Applied Physics Letters*, 91, 2007.

[24] D. R. Strachan, D. E. Smith, D. E. Smith, T.-H. Park, Michael J. Therien, D. A. Bonnell, and A. T. Johnson. Controlled fabrication of nanogaps in ambient environment for molecular electronics. *Appl. Phys. Lett.*, 86:043109, 2005.

[25] M. Rudneva, B. Gao, F. Prins, Q. Xu, H. S. J. van der Zant, and H. W. Zandbergen. In situ transmission electron microscopy imaging of electromigration in platinum nanowires. *Microscopy and Microanalysis*, 19:43–48, 2013.

[26] F. Prins, T. Hayashi, B. J. A. de Vos van Steenwijk, B. Gao, E. A. Osorio, K. Muraki, and H. S. J. van der Zant. Room-temperature stability of pt nanogaps formed by self-breaking. *Appl. Phys. Lett.*, 94:123108, 2009.

[27] J. J. Metois, J. C. Heyraud, and A. Pimpinelli. Steady-state motion of silicon islands driven by a DC current. *Surface Science*, 420:250–258, 1998.

[28] C. Tao, W. G. Cullen, and E. D. Williams. Visualizing the Electron Scattering Force in Nanostructures. *Science*, 328:736 – 740, 2010.

[29] O. Bondarchuk, W. G. Cullen, M. Degawa, and E. D. Williams. Biased Surface Fluctuations due to Current Stress. *Phys. Rev. Lett.*, 99:206801, 2007.

[30] K. F. Braun, W. H. Soe, C. F. J. Flipse, and K. H. Rieder. Electromigration of single metal atoms observed by scanning unneling microscopy. *APL*, 90:023118, 2007.

[31] Y. Girard, T. Yamamoto, and K. Watanabe. Quantum-Chemical Interpretation of Current-Induced Forces on Adatoms on Carbon Nanotubes. *J. Phys. Chem. C*, 111:12478—-12482, 2007.

[32] D. Solenov and K. A. Velizhanin. Adsorbate Transport on Graphene by Electromigration. *Phys. Rev. Lett.*, 109:095504, 2012.

[33] D. Dundas, E. J. McEniry, and T. N. Todorov. Current-driven atomic waterwheels. *Nature Nanotech.*, 4:99 – 102, 2009.

[34] T. N. Todorov and D. Dundas. Nonconservative generalized current-induced forces. *Phys. Rev. B*, 81:075416, 2010.

[35] N. Bode, S. V. Kusminskiy, R. Egger, and F. von Oppen. Scattering Theory of Current-Induced Forces in Mesoscopic Systems. *Phys. Rev. Lett.*, 107:036804, 2011.

[36] J. Lü, T. Gunst, P. Hedegård, and M. Brandbyge. Current-induced dynamics in carbon atomic contacts. *Beilstein J. Nanotechnol.*, 2:814–823, 2011.

[37] T. N. Todorov, D. Dundas, A. T. Paxton, and A. P. Horsfield. Nonconservative current-induced forces: A physical interpretation. *Beilstein J. Nanotechnol.*, 2:727–733, 2011.

[38] J. Lü, M. Brandbyge, P. Hedegård, T. N. Todorov, and D. Dundas. Current-induced atomic dynamics, instabilities, and Raman signals: Quasiclassical Langevin equation approach. *Phys. Rev. B*, 85:245444–1, 2012.

[39] J. Lü, M. Brandbyge, and P. Hedegård. Blowing the Fuse: Berry's Phase and Runaway Vibrations in Molecular Conductors. *Nano Lett.*, 10:1657 – 1663, 2010.

[40] C. Schirm, M. Matt, F. Pauly, J. C. Cuevas, P. Nielaba, and E. Scheer. A current-driven single-atom memory. *Nature Nanotech.*, 8:645 – 648, 2013.

[41] C. Sabater, C. Untiedt, and J. M. van Ruitenbeek. Evidence for non-conservative current-induced forces in the breaking of au and pt atomic chains. *Beilstein J. Nanotechnol.*, 6:2338 – 2344, 2015.

[42] K. S. Novoselov, A. K. Geim, S. V. Morozov, D. Jiang, Y. Zhang, S. V. Dubonos, I. V. Grigorieva, and A. A. Firsov. Electric Field Effect in Atomically Thin Carbon Films. *Science*, 306:666–669, 2004.

[43] A. K. Geim and K. S. Novoselov. The rise of graphene. *Nature Materials*, 6:183–191, 2007.

[44] C. Lee, X. Wei, J. W. Kysar, and J. Hone. Measurement of the Elastic Properties and Intrinsic Strength of Monolayer Graphene. *Science*, 321:385–388, 2008.

[45] Y. W. Son, M. L. Cohen, and S. G. Louie. Half-metallic graphene nanoribbons. *Nature*, 444:347–349, 2006.

[46] M. Fujita, K. Wakabayashi, K. Nakada, and K. Kusakabe. Peculiar Localized State at Zigzag Graphite Edge. *J. Phys. Soc. Jpn.*, 65:1920–1923, 1996.

[47] K. Nakada, M. Fujita, G. Dresselhaus, and M. S. Dresselhaus. Edge state in graphene ribbons: Nanometer size effect and edge shape dependence. *Phys. Rev. B*, 54:17954–17961, 1996.

[48] L. Yang, C. Park, Y. Son, M. L. Cohen, and S. Louie. Quasiparticle Energies and Band Gaps in Graphene Nanoribbons. *Phys. Rev. Lett*, 99:186801, 2007.

[49] Y.-W. Son, Cohen, M. L., and S. G. Louie. Energy gaps in graphene nanoribbons. *Phys. Rev. Lett.*, 97:216803, 2006.

[50] V. Barone, O. Hod, and G. E. Scuseria. Electronic structure and stability of semiconducting graphene nanoribbons. *Nano Lett.*, 6:2748–2754, 2006.

[51] A. Kimouche, M. M. Ervasti, R. Drost, S. Halonen, A. Harju, P. M. Joensuu, J. Sainio, and P. Liljeroth. Ultra-narrow metallic armchair graphene nanoribbons. *Nature Commun.*, 6:10177, 2015.

[52] G. Binnig and H Rohrer. Scanning tunneling microscopy. *Surface Science*, 126:236–244, 1983.

[53] G. Binnig, C. F. Quate, and Ch. Gerber. Atomic Force Microscope. *Phys. Rev. Lett.*, 56:930, 1986.

[54] P. Grünther, U. Ch. Fischer, and Dransfeld K. Scanning near-field acoustic microscopy. *Applied Physics B*, 48:89–92, 1989.

[55] Lord Kelvin. Contact electricity of metals. *Phil. Mag.*, 18:26–31, 1898.

[56] K. Besocke. An easily operable scanning tunneling microscope. *Surface Science*, 181:145–153, 1987.

[57] J. Frohn, J. F. Wolf, K. Besocke, and M. Teske. Coarse tip distance adjustment and positioner for a scanning tunneling microscope . *Review of Scientific Instruments*, 60, 1989.

[58] J. Moser, A. Barreiro, and A Bachtold. Current-induced cleaning of graphene . *Applied Physics Letters*, 91:163513, 2007.

[59] M. R. Amirzada, A. Tatzel, V. Viereck, and H. Hillmer. Surface roughness analysis of SiO2 for PECVD, PVD and IBD on different substrates. *Applied Nanoscience*, 6:215–222, 2015.

[60] M. Koch, F. Ample, C. Joachim, and L. Grill. Voltage-dependent conductance of a single graphene nanoribbon. *Nature Nanotechnology*, 7:713—-717, 2012.

[61] J. Cai, P. Ruffieux, R. Jaafar, M. Bieri, T. Braun, S. Blankenburg, M. Muoth, A. P. Seitsonen, M. Saleh, X. Feng, K. Müllen, and R. Fasel. Atomically precise bottom-up fabrication of graphene nanoribbons. *Nature*, 466:470–473, 2010.

[62] V. W. Brar, R. Decker, H. M. Solowan, Y. Wang, L. Maserati, K. T. Chan, H. Lee, C. O. Girit, A. Zettl, S. G. Louie, M. L. Cohen, and M. F. Crommie. Gate-controlled ionization and screening of cobalt adatoms on a graphene surface. *Nature Physics*, 7:43–47, 2010.

[63] A. Ishii, M. Yamamoto, H. Asano, and K. Fujiwara. DFT calculation for adatom adsorption on graphene sheet as a prototype of carbon nanotube functionalization. *Journal of Physics: Conference Series*, 100:052087, 2008.

[64] A. Basagni, F Sedona, C. A. Pignedoli, M. Cattelan, L. Nicolas, M. Casarin, and M. Sambi. Molecules-oligomers-nanowires-graphene nanoribbons: A bottom-up stepwise on-surface covalent synthesis preserving long-range order. *J. Am. Chem. Soc.*, 137:1802–1808, 2015.

[65] H. Huang, D. Wei, J. Sun, S. L. Wong, Y. P. Feng, A. H. C. Neto, and A. T. S. Wee. Spatially Resolved Electronic Structures of Atomically Precise Armchair Graphene Nanoribbons. *Scientific Reports*, 2:983, 2012.

[66] T. Dienel, S. Kawai, H. Söde, X. Feng, K. Müllen, P. Ruffieux, R. Fasel, and O. Gröning. Resolving Atomic Connectivity in Graphene Nanostructure Junctions. *Nano Letters*, 15:5185–5190, 2015.

[67] T. N. Todorov. Local heating in ballistic atomic-scale contacts. *Philosophical Magazine B*, 77:965–973, 1998.

[68] J. D. Wrigley, M. E. Twigg, and G. Ehrlich. Lattice walks by long jumps. *J. Chem. Phys*, 93:2885, 1990.

[69] T. R. Linderoth, S. Horch, E. Lægsgaard, I. Stensgaard, and F. Besenbacher. Surface Diffusion of Pt on Pt(110): Arrhenius Behavior of Long Jumps. *Phys. Rev. Lett.*, 78:4978 – 4981, 1997.

[70] J. Repp, W. Steurerand, I. Scivetti, M. Persson, L. Gross, and G. Meyer. Charge-state-dependent diffusion of individual gold adatoms on ionic thin nacl films. *Phys. Rev. Lett.*, 117:146102, 2016.

[71] O. Deniz, C. Sanchez-Sanchez, T. Dumslaff, X. Feng, A. Narita, K. Muüllen, N. Kharche, V. Meunier, R. Fasel, and P. Ruffieux. Revealing the Electronic Structure of Silicon Intercalated Armchair Graphene Nanoribbons by Scanning Tunneling Spectroscopy. *Nano Lett.*, 17:2197–2203, 2017.

[72] H. Söde, L. Talirz, O. Gröning, C. A. Pignedoli, R. Berger, X. Feng, K. Müllen, R. Fasel, and P. Ruffieux. Electronic Band Dispersion of Graphene Nanoribbons via Fourier-Transformed Scanning Tunneling Spectroscopy. *Phys. Rev. B: Condens. Matter Mater. Phys.*, 4:45429, 2015.

[73] W. Lee, K. Kim, W. Jeong, L. A. Zotti, F. Pauly, J. C. Cuevas, and P. Reddy. Heat dissipation in atomic-scale junctions. *Nature*, 498:209—212, 2013.

[74] Y. Tang, H. Zhang, Z. Shen, M. Zhao, Y. Li, and X. Dai. The electronic and diffusion properties of metal adatoms on graphene sheets: a first-principles study. *RSC Advances*, 7:33208, 2017.

[75] J. Meair, J. P. Bergfield, C. A. Stafford, and Ph. Jacquod. Local temperature of out-of-equilibrium quantum electron systems. *PRB*, 90:035407, 2014.

[76] R. Huang, Y. Sun, C. Du, T. Gao, Y. Wu, and V. Stepanyuk. Stm-mediated atom motion: a Co atom and mixed $CoCu_n$ chains on a Cu(111) surface. *Eur. Phys. J. B*, 86:429, 2013.

[77] S. Wang, L. Talirz, C. A. Pignedoli, X. Feng, K. Muellen, R. Fasel, and P. Ruffieux. Giant edge state splitting at atomically precise zigzag edges. *Nature Communications*, 7, 2015.

[78] J. M. de Voogd, M. A. van Spronsen, F. E. Kalff, B. Bryant, O. Ostojić, A. M. J. den Haan, I. M. N. Groot, T. H. Oosterkamp, A. F. Otte, and M. J. Rost. Fast and reliable pre-approach for scanning probe microscopes based on tip-sample capacitance. *Ultramicroscopy*, 181:61–69, 2017.

[79] L. A. Belyaeva, P. M. G. van Deursen, K. I. Barbetsea, and G. F. Schneider. Hydrophilicity of Graphene in Water through Transparency to Polar and Dispersive Interactions. *Advanced Materials*, 30:1703274, 2018.